

# Strong-to-Weak Spontaneous Symmetry Breaking in a $(2 + 1)$ D Transverse-Field Ising Model under Decoherence

Yi-Ming Ding,<sup>1,2,3</sup> Yuxuan Guo,<sup>4,\*</sup> Zhen Bi,<sup>5,6,†</sup> and Zheng Yan<sup>1,2,‡</sup>

<sup>1</sup>*Department of Physics, School of Science and Research Center for  
Industries of the Future, Westlake University, Hangzhou 310030, China*

<sup>2</sup>*Institute of Natural Sciences, Westlake Institute for Advanced Study, Hangzhou 310024, China*

<sup>3</sup>*State Key Laboratory of Surface Physics and Department of Physics, Fudan University, Shanghai 200438, China*

<sup>4</sup>*Department of Physics, University of Tokyo, 7-3-1 Hongo, Bunkyo-ku, Tokyo 113-0033, Japan*

<sup>5</sup>*Department of Physics, The Pennsylvania State University, University Park, Pennsylvania, 16802, USA*

<sup>6</sup>*Center for Theory of Emergent Quantum Matter, Institute for Computational and Data Sciences,  
The Pennsylvania State University, University Park, Pennsylvania, 16802, USA*

Decoherence in many-body quantum systems can give rise to intrinsically mixed-state phases and phase transitions beyond the pure-state paradigm. Here we study the  $(2 + 1)$ D transverse-field Ising model (TFIM) subject to a strongly  $\mathbb{Z}_2$ -symmetric decoherence channel, with a focus on strong-to-weak spontaneous symmetry breaking (SWSSB). This problem is challenging because the relevant transitions occur in the strong-decoherence regime, beyond the reach of perturbative expansions around the pure-state limit, while conventional quantum Monte Carlo (QMC) methods are hampered by the need to access nonlinear observables and by the sign problem. We overcome these difficulties by developing a QMC algorithm that efficiently evaluates nonlinear Rényi-2 correlators in higher dimensions, complemented by an effective field-theoretic approach. We show that the decohered state realizes a rich mixed-state phase diagram governed by an effective 2D Ashkin–Teller theory. This theory enables analytical predictions for the mixed-state phases and the universality classes of the phase boundaries, all of which are confirmed by large-scale QMC simulations.

*Introduction.-* In recent years, rapid advances in quantum simulation platforms have brought nonequilibrium quantum matter to the forefront of condensed matter physics [1–4]. In these systems, unavoidable coupling to the environment induces decoherence, which can qualitatively reshape collective behavior and give rise to novel mixed-state phases and phase transitions in interacting many-body systems [5–43]. A central question is how symmetry and symmetry breaking, a basic organizing principle of quantum phases of matter [44–46], generalize to open quantum systems. Here one must distinguish between strong and weak symmetry [47–49]. A mixed state with strong symmetry is analogous to a canonical ensemble with fixed symmetry charge, whereas a mixed state with weak symmetry is analogous to a grand-canonical ensemble, in which different symmetry charges are mixed while the full density matrix remains symmetric. Accordingly, strong symmetry has a direct pure-state analog, whereas weak symmetry is meaningful only for mixed states. This distinction gives rise to strong-to-weak spontaneous symmetry breaking (SWSSB), in which strong symmetry is lost while weak symmetry remains [6, 7, 13–17, 19–21, 23–25, 39, 40, 50–66]. It is a genuinely mixed-state form of order, with no counterpart in pure states.

Compared with conventional spontaneous symmetry breaking (SSB), diagnosing SWSSB requires nonlinear probes. Faithful order parameters include the fidelity and Rényi-1 correlators [15, 67, 68], which obey the stability theorem of two-way connectivity via symmetric short-depth quantum channels, but are generally difficult to evaluate in many-body systems. By contrast, the Rényi-2 correlator, defined through a doubled pure-

state representation via the Choi-Jamiołkowski isomorphism [69, 70], provides a practical proxy for detecting SWSSB [6, 14]. Its advantage lies in both numerical and experimental accessibility: evaluating fidelity or Rényi-1 correlators requires canonical purification and thus full state tomography, whereas phase transitions of Rényi-2 observables can be efficiently measured using modern techniques such as classical shadow tomography [17, 71, 72].

Importantly, the Rényi-2 correlator is well suited for numerical approaches such as tensor-network methods based on matrix product states (MPS) in a doubled Hilbert space [19–22]. However, these methods are largely restricted to one dimension and become challenging in higher dimensions. Quantum Monte Carlo (QMC) methods, by contrast, are naturally suited for large-scale simulations and largely independent of spatial dimension. Recent work has explored Monte Carlo sampling of SWSSB in specific models that admit classical stochastic representations [73]. However, a general QMC framework for directly computing the Rényi-2 correlator in interacting quantum systems, without relying on mapped classical representations, remains lacking. In this Letter, we develop a QMC framework for evaluating the Rényi-2 correlator, thereby filling this methodological gap and enabling unbiased large-scale simulations of decohered quantum states and SWSSB in arbitrary spatial dimensions.

As an illustrative example, we investigate the  $(2 + 1)$ D transverse-field Ising model (TFIM) subject to a strongly  $\mathbb{Z}_2$ -symmetric decoherence channel. Despite its simplicity, the mixed-state phase diagram of this system re-

mains largely unexplored except in the product-state limit [15]. By combining a field-theoretical approach with our newly developed QMC techniques, we characterize the decohered Ising ground states across various parameter regimes. Our field-theoretical framework maps the effective defect action to the (1+1)D Ashkin-Teller model [74], predicting three distinct phases and identifying the universality classes of the phase transitions as well as the tricritical point. All these analytical predictions are firmly corroborated by large-scale simulations enabled by our QMC framework.

*Setup.*- We investigate the phase diagram of the decohered ground state of the TFIM as a function of Ising interaction and decoherence strength. Specifically, we consider a  $L \times L$  2D square lattice of spins with periodic boundary conditions described by the Hamiltonian  $H = -J \sum_{\langle ij \rangle} Z_i Z_j - \sum_i X_i$ , where  $Z_i$  and  $X_i$  are Pauli operators, and  $\langle ij \rangle$  denotes the nearest-neighbor bonds. The quantum critical point is located at  $J_c \approx 0.328474$  [75], which corresponds to a 3D Ising conformal field theory (CFT). When  $J < J_c$ , the system is in a paramagnetic phase, and the ground state  $\rho_0$  has a global strong  $\mathbb{Z}_2$  symmetry under the symmetry operator  $X \equiv \prod_i X_i$ . When  $J > J_c$ , the strong  $\mathbb{Z}_2$  symmetry is spontaneously broken to the trivial group, leading to a ferromagnetic order, as characterized by the linear order parameter  $C^{(0)} \equiv \lim_{|i-j| \rightarrow \infty} \text{Tr}(\rho_0 Z_i Z_j) = O(1)$ .

By applying the decoherence channel  $\mathcal{E} = \prod_{\langle ij \rangle} \mathcal{E}_{\langle ij \rangle}$  to  $\rho_0$ , we obtain  $\rho = \mathcal{E}[\rho_0]$ , where each local channel preserves the strong  $\mathbb{Z}_2$  symmetry and is defined as

$$\mathcal{E}_{\langle ij \rangle}[\rho_0] = \left(1 - \frac{p}{2}\right) \rho_0 + \frac{p}{2} Z_i Z_j \rho_0 Z_i Z_j, \quad p \in [0, 1]. \quad (1)$$

We study the phase diagram of  $\rho$  as a function of the decoherence strength  $p$  and the coupling  $J$ . To do so, we first introduce several diagnostics for the distinct mixed-state phases.

Under the Choi-Jamiołkowski isomorphism [69, 70], density matrix  $\rho = \sum_{s,s'} \rho_{ss'} |s\rangle\langle s'|$  is mapped onto a pure state  $|\rho\rangle\rangle = \sum_{s,s'} \rho_{ss'} |s\rangle_a |s'\rangle_b^*$  in a doubled Hilbert space, where  $a$  and  $b$  label the two replicas. The symmetry of the system is given by  $(\mathbb{Z}_2^a \times \mathbb{Z}_2^b) \times \mathbb{Z}_2^H$ , where  $\mathbb{Z}_2^{a/b}$  encode the strong symmetry in doubled space, while  $\mathbb{Z}_2^H$  arises from Hermiticity and is strictly preserved. This symmetry structure allows two patterns of SSB [6]: complete breaking of  $\mathbb{Z}_2^a \times \mathbb{Z}_2^b$ , or partial breaking to the diagonal subgroup  $\mathbb{Z}_2^{\text{diag}}$ , corresponding to SWSSB. To diagnose the presence of SWSSB, we compute the Rényi-2 correlator  $C^{(2)} \equiv \lim_{|i-j| \rightarrow \infty} \text{Tr}(\rho Z_i Z_j \rho Z_i Z_j) / \text{Tr}(\rho^2)$ . A nonzero  $C^{(2)}$  signals spontaneous breaking of the strong symmetry, but by itself does not diagnose the fate of the weak symmetry in the Choi doubled space.

To distinguish between the two symmetry-broken patterns, we also introduce the *Rényi-2 linear order correlator in the doubled space*, defined as  $C^{(1)} \equiv$

$\lim_{|i-j| \rightarrow \infty} \text{Tr}(\rho^2 Z_i Z_j) / \text{Tr}(\rho^2)$ . At the Choi-state level,  $C^{(1)} = \lim_{|i-j| \rightarrow \infty} \langle\langle \rho | Z_i^{a/b} Z_j^{a/b} | \rho \rangle\rangle / \langle\langle \rho | \rho \rangle\rangle$  is the natural linear order parameter, which is nonzero only when the  $\mathbb{Z}_2^a \times \mathbb{Z}_2^b$  symmetry is completely broken, indicating the absence of weak symmetry of the original mixed state  $\rho$ .

The three correlators  $C^{(0)}$ ,  $C^{(1)}$ , and  $C^{(2)}$  probe symmetry-breaking structure with increasing sensitivity to the Choi-state representation of  $\rho$ . Among them,  $C^{(0)}$  diagnoses symmetry breaking directly at the level of the density matrix and therefore determines whether weak symmetry is broken. By contrast,  $C^{(1)}$  and  $C^{(2)}$  are nonlinear probes, sensitive to order that survives only in the doubled-state description. This clarifies the seemingly paradoxical regime  $C^{(1)} \neq 0$  but  $C^{(0)} = 0$ : the density matrix itself remains weakly symmetric, while the associated Choi state still carries a finer symmetry-breaking structure. Compared with  $C^{(0)}$ , the correlator  $C^{(1)}$  enhances the dominant contributions to  $\rho$  and thus serves as a more sensitive probe of this hidden order. However, a nonzero  $C^{(1)}$  should be understood as signaling symmetry breaking in the associated Choi doubled state, and not necessarily spontaneous symmetry breaking of the mixed state in the strict sense. We nevertheless refer to the regime with  $C^{(1)} \neq 0$  and  $C^{(0)} = 0$  as the *Rényi-2 spontaneous symmetry breaking* (R2-SSB) regime. In contrast, when  $C^{(2)} \neq 0$  but  $C^{(1)} = 0$ , the order is breaking  $\mathbb{Z}_2^{a/b}$  down to  $\mathbb{Z}_2^{\text{diag}}$  in the Choi state; we call this the *Rényi-2 strong-to-weak spontaneous symmetry breaking* (R2-SWSSB) regime. Thus, the hierarchy of  $C^{(0)}$ ,  $C^{(1)}$ , and  $C^{(2)}$  distinguishes ordinary symmetry breaking of  $\rho$  from progressively finer symmetry-breaking in its Choi-state representation. A systematic review of these diagnostics is provided in the Supplemental Material [76].

*Quantum Monte Carlo method.*- Although the finite-temperature Gibbs state or ground state of a quantum Hamiltonian can be efficiently simulated using standard QMC methods based on imaginary-time path integral or series expansion [77–85], directly implementing the local channel  $\mathcal{E}_{\langle ij \rangle}$  is nontrivial. In spin-1/2 models, the computational basis is typically chosen as the local  $Z$  basis  $\{|s\rangle\}$  with  $s \in \{0, 1\}^{\otimes N}$ , where  $|0\rangle \equiv |\uparrow\rangle$  and  $|1\rangle \equiv |\downarrow\rangle$ . The difficulty arises because operators such as  $Z_i Z_j$  in Eq. (1), when acting within this computational basis, generically induce the notorious sign problem.

To circumvent this issue, we rewrite the local channel  $\mathcal{E}_{\langle ij \rangle}$  in Eq. (1) as  $\mathcal{E}_{\langle ij \rangle}[\rho_0] = \sum_k M_k \rho_0 M_k^\dagger$ , where

$$\begin{aligned} M_0 &= \sqrt{1-p} \mathbb{1}_i \mathbb{1}_j, \\ M_1 &= \sqrt{p} \frac{\mathbb{1}_i \mathbb{1}_j + Z_i Z_j}{2}, \quad M_2 = \sqrt{p} \frac{\mathbb{1}_i \mathbb{1}_j - Z_i Z_j}{2}. \end{aligned} \quad (2)$$

Then, the action of  $\mathcal{E}_{\langle ij \rangle}$  on a general density matrix  $\rho_0 = \sum_{s,s'} \langle s | \rho_0 | s' \rangle |s\rangle\langle s'|$  can be written as  $\mathcal{E}_{\langle ij \rangle}[\rho_0] = \sigma_1 + \sigma_2$ ,

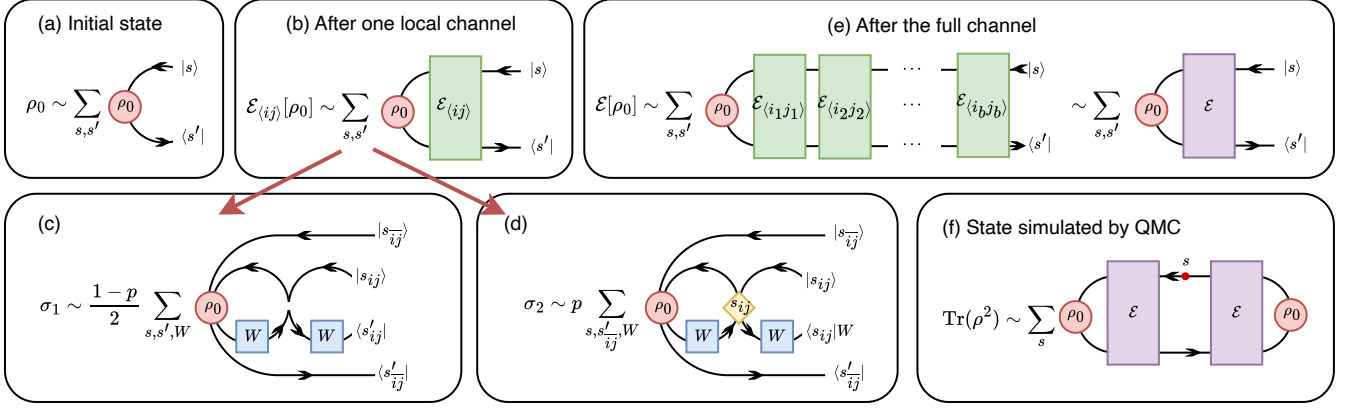


FIG. 1. Graphical representation of the density matrix in the evolution picture, with propagation from the ket to the bra index in the computational basis. (a) Initial state  $\rho_0$ . (b) State after a single local channel. (c, d) Two contributions  $\sigma_1$  and  $\sigma_2$  in  $\mathcal{E}_{\langle ij \rangle}[\rho_0] = \sigma_1 + \sigma_2$  shown in (b). The yellow diamond in (d) denotes a Kronecker tensor enforcing identical spin states on sites  $i$  and  $j$  along four time directions. (e) State after the full channel. (f) Contracting two copies of  $\rho = \mathcal{E}[\rho_0]$  yields  $\rho^2$ . Further contracting the bra and ket indices gives  $\text{Tr}(\rho^2)$ , which can be simulated by QMC to evaluate Rényi-2 observables.

where

$$\sigma_1 \equiv \frac{1-p}{2} \sum_s \sum_{s'} \sum_W \langle s | \rho_0 W W | s' \rangle |s\rangle \langle s'|, \quad (3)$$

$$\sigma_2 \equiv p \sum_s \sum_{s'_{ij}} \sum_W \langle s | \rho_0 W | s_{ij}, s'_{ij} \rangle |s\rangle \langle s_{ij}, s'_{ij} | W, \quad (4)$$

and  $W \in \{\mathbb{1}_i \mathbb{1}_j, X_i X_j\}$ . For convenience, we decompose each basis state  $|s\rangle = \otimes_k |s_k\rangle$  as  $|s\rangle \equiv |s_{ij}\rangle \otimes |s_{\bar{i}\bar{j}}\rangle$ , where  $|s_{ij}\rangle \equiv |s_i\rangle \otimes |s_j\rangle$  denotes the local degrees of freedom on sites  $i$  and  $j$ , and  $|s_{\bar{i}\bar{j}}\rangle \equiv \otimes_{k \neq i,j} |s_k\rangle$  represents the remaining degrees of freedom. A more detailed derivation of Eqs. (3) and (4) can be found in the Supplemental Material [76].

The essential idea of QMC is to sample matrix elements of  $\rho_0 \propto e^{-\beta H}$  with weights  $W_{s,s'} \propto \langle s | \rho_0 | s' \rangle$ , without storing the full density matrix [30, 86–88]. As  $\rho_0$  represents imaginary-time evolution [Fig. 1(a)], different matrix elements correspond to different temporal boundary conditions. In particular, sampling  $\langle s | \rho_0 | s \rangle$  imposes periodic boundary conditions by identifying the bra and ket states, yielding the standard partition function  $Z = \text{Tr}(e^{-\beta H})$ . We note that matrix elements in  $\sigma_1$  and  $\sigma_2$  can be interpreted similarly [Fig. 1(b)-(d)]. Without loss of generality, we choose a counterclockwise time orientation. For  $\sigma_2$ , the resulting time contour for  $s_{ij}$  has a figure-eight topology, and the orientation is taken along the outer loop. The four-leg vertices in Fig. 1(d) connect spin variables of sites  $i$  and  $j$  on different time branches and correspond to a rank-four Kronecker tensor.

By iteratively applying the local channel  $\mathcal{E}_{\langle ij \rangle}$ , one obtains the decohered state  $\rho = \mathcal{E}[\rho_0]$ , whose matrix elements admit a similar graphical representation, as illustrated in Fig. 1(e). In the same spirit, one may consider  $\rho^2 = (\mathcal{E}[\rho_0])^2$ . Imposing periodic boundary conditions

along the time direction then allows the quantity  $\text{Tr}(\rho^2)$  to be interpreted as a generalized path integral and evaluated within QMC, as shown in Fig. 1(f). Particularly, the quantities  $C^{(1)}$  and  $C^{(2)}$  for diagnosing SWSSB can be estimated using simple diagonal measurements by simulating  $\text{Tr}(\rho^2)$ . Further details, including a discussion of the polynomial (and thus efficient) complexity of our algorithm, are provided in the Supplemental Material [76].

Finally, we emphasize that the QMC framework introduced here is general and applies to any initial state  $\rho_0$  that can be prepared with standard QMC methods, including Gibbs states, ground states, and mixed states obtained by tracing out environmental degrees of freedom, and is not restricted to the TFIM considered here.

**Phase diagram and field theory analysis.**— Using the diagnostics introduced above, we map out the phase diagram of the model in the plane of Ising interaction and decoherence strength. As shown in Fig. 2, the model exhibits a rich phase structure, including a strongly symmetric phase, an R2-SWSSB phase, an R2-SSB phase, and an ordinary SSB phase. We note that the ground-state ordered region  $J > J_c$  is not destroyed by the decoherence considered here (see the discussion in the End Matter). All phase boundaries are continuous transitions. In particular, the symmetric-to-R2-SWSSB boundary and the R2-SWSSB-to-R2-SSB boundary are both in the 2D Ising universality class. Moreover, the two phase transitions merge in part of the phase diagram into a critical line with continuously varying exponents.

To determine the phase boundaries, we consider the generalized Binder ratios [89]. For example, the Binder ratio associated with  $C^{(2)}$  is defined as

$$R^{(2)} \equiv \frac{\sum_{i,j,k,l} \text{Tr}(\rho Z_i Z_j Z_k Z_l \rho Z_i Z_j Z_k Z_l)}{[\sum_{i,j} \text{Tr}(\rho Z_i Z_j \rho Z_i Z_j)]^2}. \quad (5)$$

Crossings of  $R^{(2)}$  for different system sizes locate the critical point. If the strong  $\mathbb{Z}_2$  symmetry is preserved,  $R^{(2)} \rightarrow 3$ , whereas  $R^{(2)} \rightarrow 1$  when it is broken. Similar ratios  $R^{(\alpha)}$  can be defined for other  $C^{(\alpha)}$  using the corresponding two- and four-point correlators.

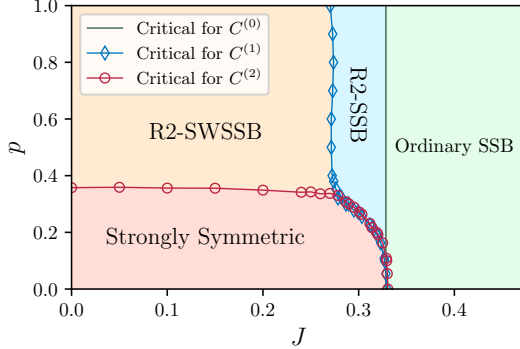


FIG. 2. Phase diagram of the decohered ground state of the 2D TFIM under the quantum channel  $\mathcal{E}$ . Markers denote critical points obtained from QMC simulations associated with the corresponding order parameters. For ground-state preparation, we take  $\beta = 2L$ , and verify convergence. The strongly symmetric phase is characterized by  $C^{(\alpha)} = 0$  for  $\alpha = 0, 1, 2$ ; the R2-SWSSB phase by  $C^{(2)} \neq 0$  and  $C^{(0)} = C^{(1)} = 0$ ; the R2-SSB phase by  $C^{(1)}, C^{(2)} \neq 0$  with  $C^{(0)} = 0$ ; and the ordinary SSB phase by  $C^{(\alpha)} \neq 0$  for all  $\alpha = 0, 1, 2$ .

We perform finite-size scaling to determine the universality classes of the phase boundaries in Fig. 2. Before the red and blue boundaries merge, we find that the correlation-length exponent  $\nu$  along both boundaries is consistent with the 2D Ising universality class. Fig. 3(a) shows an example at  $J = 0.1$ , where tuning  $p$  crosses the red critical boundary at  $p_c \approx 0.355$ . Finite-size scaling yields an excellent data collapse with  $\nu \approx 0.998 \approx 1$  [Fig. 3(b)]. Similar behavior is observed for the other phase boundary, and a representative example is presented in the End Matter. By contrast, as the two boundaries merge, the critical behavior changes qualitatively, with the correlation-length exponent deviating from the Ising value (as will be demonstrated below). To understand these results, we next develop an effective field-theoretical analysis.

One can formulate the problem of decoherence on the ground state of the TFIM in the path-integral formalism, where the ground state is prepared by imaginary-time evolution and the decoherence is encoded as an interaction along a codimension-one temporal defect [6, 90]. This leads to the effective action

$$S_{\text{eff}}[\phi_a, \phi_b] = S_{\text{Ising}}[\phi_a] + S_{\text{Ising}}[\phi_b] + S_{\text{int}}[\phi_a, \phi_b]. \quad (6)$$

The bulk corresponds to a standard  $\phi^4$  action

$$S_{\text{Ising}}[\phi] = \frac{1}{2} \int d^2x dz (\partial_\mu \phi \partial^\mu \phi + m^2 \phi^2 + \lambda \phi^4), \quad (7)$$

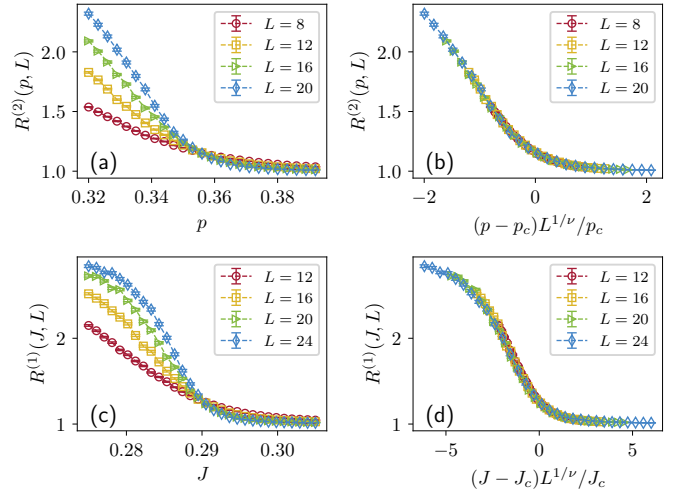


FIG. 3. Binder ratios  $R^{(\alpha)}$  as functions of system size  $L$  and tuning parameters  $J$  or  $p$ . (a) At fixed  $J = 0.1$ , the curves cross at  $p_c \approx 0.355$ . (b) Corresponding data collapse of  $R^{(2)}(p, L)$ , yielding  $\nu \approx 0.998 \approx 1$ . (c) At fixed  $p = 0.3$ , the crossing occurs at  $J_c \approx 0.29$ , close to the tricritical point. (d) Data collapse using the expected exponent  $\nu = 2/3$ , with all curves collapsing near criticality, in agreement with theory.

while the interaction induced by the decoherence only exists on a temporal defect:

$$S_{\text{int}}[\phi_a, \phi_b] = -\frac{1}{2} \int d^2x dz \delta(z) [\tilde{m} (\phi_a^2 + \phi_b^2) + t \phi_a^2 \phi_b^2]. \quad (8)$$

This interaction arises from coarse-graining the microscopic interaction in the doubled space coming from the decoherence  $V_{\text{int}} = 2\delta(z) \tanh^{-1}[p/(2-p)] \sum_{(i,j)} Z_i^a Z_j^a Z_i^b Z_j^b$ , implying  $\tilde{m}, t \propto \tanh^{-1}[p/(2-p)]$ , see Supplemental Material [76] for a detailed derivation.

In the bulk ordered phase ( $m^2 < 0$ ), the  $\mathbb{Z}_2^a \times \mathbb{Z}_2^b$  symmetry is broken completely, and the resulting order is stable against symmetric finite-depth quantum channels. The system therefore lies in an ordinary SSB phase. In contrast, when the bulk is disordered ( $m^2 > 0$ ), its finite correlation length implies that the bulk induces only short-range interactions on the defect, allowing for a much richer defect phase structure tuned by decoherence. The corresponding effective theory is equivalent to that of the 2D Ashkin-Teller model:

$$S_{\text{eff}}[\varphi_a, \varphi_b] = \int d^2x \left[ \frac{1}{2} \sum_{\alpha=a,b} (\partial_\mu \varphi^\alpha \partial^\mu \varphi^\alpha + m_{\text{eff}}^2 \varphi_\alpha^2 + \tilde{\lambda} \varphi_\alpha^4) - \tilde{t} \varphi_a^2 \varphi_b^2 \right] + \dots \quad (9)$$

where  $m_{\text{eff}}^2 = m(2m - \tilde{m})$ ,  $\tilde{\lambda} = \lambda m/2$  and  $\tilde{t} = t m^2$ . We explicitly demonstrate this by integrating out the bulk fields in the path integral; detailed derivations are provided in the Supplemental Material [76].

In the bulk disordered phase, the effective 2D Ashkin-Teller action (9) captures three distinct phases

(see Supplemental Material [76] for a Landau–Ginzburg analysis). For  $m_{\text{eff}}^2 > 0$  and  $t$  is small compared to  $\lambda/m$ , no symmetry is broken, and the system is in a trivial symmetric phase. When  $m_{\text{eff}}^2 < 0$  and the inter-replica coupling  $t$  is relatively small compared to  $\lambda/m$ , the Ashkin–Teller model enters the ferromagnetic phase (R2-SSB). This corresponds to the complete breaking of the  $\mathbb{Z}_2^a \times \mathbb{Z}_2^b$  symmetry to the trivial group. The third regime is the Baxter phase (R2-SWSSB), which emerges when  $t$  is sufficiently large. In this phase, the  $\mathbb{Z}_2^a \times \mathbb{Z}_2^b$  symmetry is partially broken down to the diagonal subgroup  $\mathbb{Z}_2^{\text{diag}}$ . In particular, this field-theoretical analysis accounts for the meeting of these three phases at a tricritical point, in excellent agreement with the phase diagram in Fig. 2.

Within the 2D Ashkin–Teller description, the transitions from the trivial to the Baxter phase (red boundary in Fig. 2) and from the Baxter to the ferromagnetic phase (blue boundary) correspond to sequential breaking of two independent  $\mathbb{Z}_2$  symmetries. Both transitions thus belong to the 2D Ising universality class, consistent with our numerical results. More intriguingly, the direct transition between the strongly symmetric and R2-SSB phases (where the red and blue boundaries overlap in Fig. 2) is governed by a compact boson CFT with a continuously tunable parameter, leading to continuously varying critical exponents along the phase boundary. Representative numerical results are presented in the End Matter.

Furthermore, the tricritical point where the strongly symmetric, R2-SWSSB, and R2-SSB phases meet is described by the 2D 4-state Potts CFT [91]. The critical behavior is governed by the leading relevant energy-density operator  $\varepsilon$  with scaling dimension  $\Delta_\varepsilon = 1/2$ , yielding  $\nu = 1/(2 - \Delta_\varepsilon) = 2/3$ , while the subleading operator  $\varepsilon'$  is marginal with  $\Delta_{\varepsilon'} = 2$ . Although the tricritical point is difficult to locate precisely, data in its vicinity [Fig. 3(c), (d)] exhibit an excellent collapse with the expected exponent, supporting the Potts CFT description.

When  $S_{\text{Ising}}$  is tuned to the critical point, the bulk correlation length diverges, which induces long-range interactions on the defect, invalidating the Ashkin–Teller description. Instead, this regime can be analyzed using conformal perturbation theory. Additional details and numerical confirmation are provided in the End Matter.

**Conclusions and outlook.**— In this Letter, we propose a general QMC framework for evaluating nonlinear Rényi-2 correlators in decohered quantum many-body systems, filling a key methodological gap and enabling unbiased large-scale simulations of SWSSB in higher dimensions. Combined with effective field-theoretical analysis, we systematically study the  $(2 + 1)$ D TFIM under a strongly  $\mathbb{Z}_2$ -symmetric decoherence channel, revealing a rich mixed-state phase diagram with three distinct phases: a strongly symmetric phase, a R2-SWSSB phase with partial symmetry breaking, and an R2-SSB phase with complete symmetry breaking in the doubled space.

Our field-theoretical approach provides a unified un-

derstanding of these phases and their transitions. Away from the Ising quantum critical point, the effective defect theory is governed by the 2D Ashkin–Teller model, leading to Ising-type transitions, a line of continuously varying criticality described by a compact boson CFT, and a tricritical point in the 2D 4-state Potts universality class. At the underlying quantum critical point, decoherence acts as a relevant defect perturbation, immediately driving the system into the R2-SSB phase with distinct critical scaling. These analytical predictions are in quantitative agreement with our QMC results.

Experimentally, both the TFIM and Pauli channels can be realized in quantum simulators [92–96]. Notably, SWSSB has recently been observed through Rényi- $k$  correlators using quantum gas microscopy [97]. Replica-based and randomized-measurement protocols also provide routes to the Rényi-2 diagnostics studied here [17, 98–100].

Beyond the present model, our QMC and field theory framework opens several promising directions. It enables unbiased large-scale studies of mixed-state phases and phase transitions in a broad class of interacting systems, including higher dimensions, frustration, topological order, and continuous symmetries. It also naturally generalizes to a wide range of decoherence channels, including those preserving strong continuous symmetries and combinations of distinct channels. Moreover, combined with recent advances in QMC [101–108], our framework can be extended to other nonlinear probes, such as entanglement entropy [8, 109], entanglement Rényi negativity [8, 13, 110, 111], coherent information [13, 112], and (conditional) mutual information [23], implemented via appropriate spacetime boundary conditions among replicas based on the graphical evolution picture introduced here. These capabilities provide a powerful route to uncover and characterize new forms of mixed-state collective phenomena in the future.

**Acknowledgments.**— We thank Chong Wang, Yijian Zou, Yuto Ashida and Liujun Zou for helpful discussions. Y.G. is financially supported by the Global Science Graduate Course (GSGC) program at the University of Tokyo. This project is supported by the Scientific Research Project (No. WU2025B011), Feng-Ying Career Development Chair Fund and the Start-up Fund of Westlake University. Z.B. acknowledges support from NSF CAREER Grant No. DMR-2339319. The authors thank the IT service office and the high-performance computing center of Westlake University.

**Note added.**— After completion of this work, we became aware of a parallel, independent, and complementary work by Z. Weinstein and S. J. Garratt [113], which addresses the dual problem, the decoding problem in the  $(2 + 1)$ D transverse-field toric code under decoherence, using a distinct approach.

**Data availability.**— The data supporting this work are publicly available on Zenodo [114].

- 
- \* yuanguo2024@g.ecc.u-tokyo.ac.jp  
† zjb5184@psu.edu  
‡ zhengyan@westlake.edu.cn
- [1] I. M. Georgescu, S. Ashhab, and F. Nori, Quantum simulation, *Rev. Mod. Phys.* **86**, 153 (2014).
  - [2] M. Saffman, Quantum computing with neutral atoms, *National Science Review* **6**, 24 (2018), <https://academic.oup.com/nsr/article-pdf/6/1/24/38915067/nwy088.pdf>.
  - [3] J. Preskill, Quantum computing in the nisq era and beyond, *Quantum* **2**, 79 (2018).
  - [4] B. Zeng, X. Chen, D.-L. Zhou, and X.-G. Wen, in *Quantum Information Meets Quantum Matter: From Quantum Entanglement to Topological Phases of Many-Body Systems* (Springer New York, New York, NY, 2019).
  - [5] J. Y. Lee, Y.-Z. You, and C. Xu, Symmetry protected topological phases under decoherence, *Quantum* **9**, 1607 (2025), [arXiv:2210.16323 \[cond-mat.str-el\]](https://arxiv.org/abs/2210.16323).
  - [6] J. Y. Lee, C.-M. Jian, and C. Xu, Quantum criticality under decoherence or weak measurement, *PRX Quantum* **4**, 030317 (2023).
  - [7] R. Ma and C. Wang, Average symmetry-protected topological phases, *Phys. Rev. X* **13**, 031016 (2023).
  - [8] Y. Zou, S. Sang, and T. H. Hsieh, Channeling quantum criticality, *Phys. Rev. Lett.* **130**, 250403 (2023).
  - [9] A. Moharramipour, L. A. Lessa, C. Wang, T. H. Hsieh, and S. Sahu, Symmetry-enforced entanglement in maximally mixed states, *PRX Quantum* **5**, 040336 (2024).
  - [10] K. Su, N. Myerson-Jain, C. Wang, C.-M. Jian, and C. Xu, Higher-form symmetries under weak measurement, *Phys. Rev. Lett.* **132**, 200402 (2024).
  - [11] Y. Guo and Y. Ashida, Two-dimensional symmetry-protected topological phases and transitions in open quantum systems, *Phys. Rev. B* **109**, 195420 (2024).
  - [12] Z. Yan, L. Pollet, J. Lou, X. Wang, Y. Chen, and Z. Cai, Interacting lattice systems with quantum dissipation: A quantum monte carlo study, *Phys. Rev. B* **97**, 035148 (2018).
  - [13] R. Fan, Y. Bao, E. Altman, and A. Vishwanath, Diagnostics of mixed-state topological order and breakdown of quantum memory, *PRX Quantum* **5**, 020343 (2024).
  - [14] P. Sala, S. Gopalakrishnan, M. Oshikawa, and Y. You, Spontaneous strong symmetry breaking in open systems: Purification perspective, *Phys. Rev. B* **110**, 155150 (2024).
  - [15] L. A. Lessa, R. Ma, J.-H. Zhang, Z. Bi, M. Cheng, and C. Wang, Strong-to-weak spontaneous symmetry breaking in mixed quantum states, *PRX Quantum* **6**, 010344 (2025).
  - [16] C. Zhang, Y. Xu, J.-H. Zhang, C. Xu, Z. Bi, and Z.-X. Luo, Strong-to-weak spontaneous breaking of 1-form symmetry and intrinsically mixed topological order, *Phys. Rev. B* **111**, 115137 (2025).
  - [17] N. Sun, P. Zhang, and L. Feng, Scheme to detect the strong-to-weak symmetry breaking via randomized measurements, *Phys. Rev. Lett.* **135**, 090403 (2025).
  - [18] B. Min, Y. Zhang, Y. Guo, D. Segal, and Y. Ashida, Mixed-state phase transitions in spin-holstein models, *Phys. Rev. B* **111**, 115123 (2025).
  - [19] Y. Guo, S. Yang, and X.-J. Yu, Quantum strong-to-weak spontaneous symmetry breaking in decohered one-dimensional critical states, *PRX Quantum* **6**, 040311 (2025).
  - [20] Y. Guo and S. Yang, Strong-to-weak spontaneous symmetry breaking meets average symmetry-protected topological order, *Phys. Rev. B* **111**, L201108 (2025).
  - [21] T. Orito, Y. Kuno, and I. Ichinose, Strong and weak symmetries and their spontaneous symmetry breaking in mixed states emerging from the quantum ising model under multiple decoherence, *Phys. Rev. B* **111**, 054106 (2025).
  - [22] Y. Guo and S. Yang, Quantum criticality in open quantum systems from the purification perspective (2026), [arXiv:2602.21979 \[quant-ph\]](https://arxiv.org/abs/2602.21979).
  - [23] S. Sang and T. H. Hsieh, Stability of mixed-state quantum phases via finite markov length, *Phys. Rev. Lett.* **134**, 070403 (2025).
  - [24] L. Chen, N. Sun, and P. Zhang, Strong-to-weak symmetry breaking and entanglement transitions, *Phys. Rev. B* **111**, L060304 (2025).
  - [25] R. Ma and A. Turzillo, Symmetry-protected topological phases of mixed states in the doubled space, *PRX Quantum* **6**, 010348 (2025).
  - [26] R. Ma, J.-H. Zhang, Z. Bi, M. Cheng, and C. Wang, Topological phases with average symmetries: The decohered, the disordered, and the intrinsic, *Phys. Rev. X* **15**, 021062 (2025).
  - [27] Y. Guo, J.-H. Zhang, H.-R. Zhang, S. Yang, and Z. Bi, Locally purified density operators for symmetry-protected topological phases in mixed states, *Phys. Rev. X* **15**, 021060 (2025).
  - [28] T. D. Ellison and M. Cheng, Toward a classification of mixed-state topological orders in two dimensions, *PRX Quantum* **6**, 010315 (2025).
  - [29] L. A. Lessa, M. Cheng, and C. Wang, Mixed-state quantum anomaly and multipartite entanglement, *Phys. Rev. X* **15**, 011069 (2025).
  - [30] Y.-M. Ding, Z. Liu, X. Tian, Z. Wang, Y. Zhu, and Z. Yan, Mixed-state measurement-induced phase transitions in imaginary-time dynamics (2026), [arXiv:2511.04402 \[quant-ph\]](https://arxiv.org/abs/2511.04402).
  - [31] S. Sang, Y. Zou, and T. H. Hsieh, Mixed-state quantum phases: Renormalization and quantum error correction, *Phys. Rev. X* **14**, 031044 (2024).
  - [32] T. Rakovszky, S. Gopalakrishnan, and C. von Keyserlingk, Defining stable phases of open quantum systems, *Phys. Rev. X* **14**, 041031 (2024).
  - [33] S. Sang, L. A. Lessa, R. S. K. Mong, T. Grover, C. Wang, and T. H. Hsieh, Mixed-state phases from local reversibility (2025), [arXiv:2507.02292 \[quant-ph\]](https://arxiv.org/abs/2507.02292).
  - [34] M. B. Hastings, Topological order at nonzero temperature, *Phys. Rev. Lett.* **107**, 210501 (2011).
  - [35] Z. Wang and L. Li, Anomaly in open quantum systems and its implications on mixed-state quantum phases, *PRX Quantum* **6**, 010347 (2025).
  - [36] P.-S. Hsin, Z.-X. Luo, and H.-Y. Sun, Anomalies of average symmetries: entanglement and open quantum systems, *Journal of High Energy Physics* **2024**, 134 (2024).
  - [37] Y. Xu and C.-M. Jian, Average-exact mixed anomalies and compatible phases, *Phys. Rev. B* **111**, 125128 (2025).
  - [38] L. Li, Z. Bi, and W. Cao, Generalized symmetry-protected topological phases in mixed states from gauging dualities (2026), [arXiv:2603.17282 \[cond-mat.str-el\]](https://arxiv.org/abs/2603.17282).
  - [39] N. Ziereis, S. Moudgalya, and M. Knap, Strong-to-

- weak symmetry breaking phases in steady states of quantum operations (2025), [arXiv:2509.09669 \[cond-mat.stat-mech\]](#).
- [40] L. Sá and B. Béri, Exactly solvable dissipative dynamics and one-form strong-to-weak spontaneous symmetry breaking in interacting two-dimensional spin systems, *Phys. Rev. B* **112**, 144311 (2025).
- [41] Q. Wang, R. Vasseur, S. Trebst, A. W. W. Ludwig, and G.-Y. Zhu, [Decoherence-induced self-dual criticality in topological states of matter](#) (2025), [arXiv:2502.14034 \[quant-ph\]](#).
- [42] S.-T. Zhou, M. Cheng, T. Rakovszky, C. von Keyserlingk, and T. D. Ellison, Finite-temperature quantum topological order in three dimensions, *Phys. Rev. Lett.* **135**, 040402 (2025).
- [43] M. Pütz, S. J. Garratt, H. Nishimori, S. Trebst, and G.-Y. Zhu, [Learning transitions in classical ising models and deformed toric codes](#) (2025), [arXiv:2504.12385 \[cond-mat.stat-mech\]](#).
- [44] L. D. Landau, On the theory of phase transitions. I., *Phys. Z. Sowjet.* **11**, 26 (1937).
- [45] S. Sachdev, *Quantum Phase Transitions*, 2nd ed. (Cambridge University Press, 2011).
- [46] J. McGreevy, Generalized symmetries in condensed matter, *Annual Review of Condensed Matter Physics* **14**, 57 (2023).
- [47] B. Buča and T. Prosen, A note on symmetry reductions of the lindblad equation: transport in constrained open spin chains, *New Journal of Physics* **14**, 073007 (2012).
- [48] V. V. Albert and L. Jiang, Symmetries and conserved quantities in lindblad master equations, *Phys. Rev. A* **89**, 022118 (2014).
- [49] S. Lieu, R. Belyansky, J. T. Young, R. Lundgren, V. V. Albert, and A. V. Gorshkov, Symmetry breaking and error correction in open quantum systems, *Phys. Rev. Lett.* **125**, 240405 (2020).
- [50] Y. Bao, R. Fan, A. Vishwanath, and E. Altman, Mixed-state topological order and the errorfield double formulation of decoherence-induced transitions, [arXiv](#) (2023), [2301.05687](#).
- [51] O. Ogunnaike, J. Feldmeier, and J. Y. Lee, Unifying Emergent Hydrodynamics and Lindbladian Low-Energy Spectra across Symmetries, Constraints, and Long-Range Interactions, *Phys. Rev. Lett.* **131**, 220403 (2023), [arXiv:2304.13028 \[cond-mat.str-el\]](#).
- [52] J.-H. Zhang, C. Xu, and Y. Xu, [Fluctuation-dissipation theorem and information geometry in open quantum systems](#) (2024), [arXiv:2409.18944 \[quant-ph\]](#).
- [53] J. Kim, E. Altman, and J. Y. Lee, [Error threshold of syk codes from strong-to-weak parity symmetry breaking](#) (2024), [arXiv:2410.24225 \[quant-ph\]](#).
- [54] S. Lu, P. Zhu, and Y.-M. Lu, [Bilayer construction for mixed state phenomena with strong, weak symmetries and symmetry breakings](#) (2024), [arXiv:2411.07174 \[cond-mat.str-el\]](#).
- [55] D. Gu, Z. Wang, and Z. Wang, [Spontaneous symmetry breaking in open quantum systems: strong, weak, and strong-to-weak](#) (2024), [arXiv:2406.19381 \[quant-ph\]](#).
- [56] Y. Kuno, T. Orito, and I. Ichinose, Strong-to-weak symmetry breaking states in stochastic dephasing stabilizer circuits, *Phys. Rev. B* **110**, 094106 (2024).
- [57] X. Huang, M. Qi, J.-H. Zhang, and A. Lucas, Hydrodynamics as the effective field theory of strong-to-weak spontaneous symmetry breaking, *Phys. Rev. B* **111**, 125147 (2025).
- [58] R. Luo, Y.-N. Wang, and Z. Bi, Topological holography for mixed-state phases and phase transitions, *PRX Quantum* **6**, 040358 (2025).
- [59] Y. Liu and Y. Zou, [Polynomial-time certification of fidelity for many-body mixed states and mixed-state universality classes](#) (2026), [arXiv:2601.13333 \[quant-ph\]](#).
- [60] Y. Zhang, T. H. Hsieh, Y. B. Kim, and Y. Zou, [Probing mixed-state phases on a quantum computer via renyi correlators and variational decoding](#) (2025), [arXiv:2505.02900 \[quant-ph\]](#).
- [61] J.-H. Zhang, Y. Qi, and Z. Bi, [Fidelity strange correlators for average symmetry-protected topological phases](#) (2025), [arXiv:2210.17485 \[cond-mat.str-el\]](#).
- [62] Z. Song and J.-H. Zhang, [Strong-to-weak spontaneous symmetry breaking of higher-form non-invertible symmetries in kitaev's quantum double model](#) (2025), [arXiv:2509.24179 \[quant-ph\]](#).
- [63] X. Feng, Z. Cheng, and M. Ippoliti, Hardness of observing strong-to-weak symmetry breaking, *Phys. Rev. Lett.* **135**, 200402 (2025).
- [64] J. Hauser, K. Su, H. Ha, J. Lloyd, T. G. Kiely, R. Vasseur, S. Gopalakrishnan, C. Xu, and M. P. A. Fisher, [Strong-to-weak symmetry breaking in open quantum systems: From discrete particles to continuum hydrodynamics](#) (2026), [arXiv:2602.16045 \[quant-ph\]](#).
- [65] C. Shu, K. Zhang, and K. Sun, [Universal dynamical scaling of strong-to-weak spontaneous symmetry breaking in open quantum systems](#) (2026), [arXiv:2603.06363 \[cond-mat.mes-hall\]](#).
- [66] Y.-H. Chen and T. Grover, [Zipping many-body quantum states: a scalable approach to diagonal entropy](#) (2025), [arXiv:2502.18898 \[quant-ph\]](#).
- [67] Z. Weinstein, Efficient detection of strong-to-weak spontaneous symmetry breaking via the rényi-1 correlator, *Phys. Rev. Lett.* **134**, 150405 (2025).
- [68] Z. Liu, L. Chen, Y. Zhang, S. Zhou, and P. Zhang, Diagnosing strong-to-weak symmetry breaking via wightman correlators, *Communications Physics* **8**, 274 (2025).
- [69] M.-D. Choi, Completely positive linear maps on complex matrices, *Linear Algebra and its Applications* **10**, 285 (1975).
- [70] A. Jamiołkowski, Linear transformations which preserve trace and positive semidefiniteness of operators, *Reports on Mathematical Physics* **3**, 275 (1972).
- [71] S. Aaronson and G. N. Rothblum, Gentle measurement of quantum states and differential privacy, in *Proceedings of the 51st Annual ACM SIGACT Symposium on Theory of Computing*, STOC 2019 (Association for Computing Machinery, New York, NY, USA, 2019) p. 322–333.
- [72] H.-Y. Huang, R. Kueng, and J. Preskill, Predicting many properties of a quantum system from very few measurements, *Nature Physics* **16**, 1050 (2020).
- [73] J. Hauser, K. Su, H. Ha, J. Lloyd, T. G. Kiely, R. Vasseur, S. Gopalakrishnan, C. Xu, and M. P. A. Fisher, [Strong-to-weak symmetry breaking in open quantum systems: From discrete particles to continuum hydrodynamics](#) (2026), [arXiv:2602.16045 \[quant-ph\]](#).
- [74] M. Kohmoto, M. den Nijs, and L. P. Kadanoff, Hamiltonian studies of the  $d = 2$  ashkin-teller model, *Phys. Rev. B* **24**, 5229 (1981).
- [75] H. W. J. Blöte and Y. Deng, Cluster monte carlo simulation of the transverse ising model, *Phys. Rev. E* **66**,

- 066110 (2002).
- [76] See Supplemental Material for the derivation of  $\sigma_1$  and  $\sigma_2$ , details of the QMC algorithm, and the field-theoretical derivation of the 2D defect action, which includes Refs. [78, 79, 82, 118–121].
- [77] N. Prokof'ev and B. Svistunov, “worm” algorithm in quantum monte carlo simulations, *Physics Letters A* **238**, 253 (1998).
- [78] A. W. Sandvik, Stochastic series expansion method with operator-loop update, *Phys. Rev. B* **59**, R14157 (1999).
- [79] A. W. Sandvik, Stochastic series expansion method for quantum ising models with arbitrary interactions, *Phys. Rev. E* **68**, 056701 (2003).
- [80] O. F. Syljuåsen and A. W. Sandvik, Quantum monte carlo with directed loops, *Phys. Rev. E* **66**, 046701 (2002).
- [81] M. Boninsegni, N. Prokof'ev, and B. Svistunov, Worm algorithm for continuous-space path integral monte carlo simulations, *Phys. Rev. Lett.* **96**, 070601 (2006).
- [82] R. G. Melko, Stochastic series expansion quantum monte carlo, in *Strongly Correlated Systems: Numerical Methods*, edited by A. Avella and F. Mancini (Springer Berlin Heidelberg, Berlin, Heidelberg, 2013) pp. 185–206.
- [83] Z. Yan, Y. Wu, C. Liu, O. F. Syljuåsen, J. Lou, and Y. Chen, Sweeping cluster algorithm for quantum spin systems with strong geometric restrictions, *Phys. Rev. B* **99**, 165135 (2019).
- [84] Z. Yan, Global scheme of sweeping cluster algorithm to sample among topological sectors, *Phys. Rev. B* **105**, 184432 (2022).
- [85] Z. Yan, R. Samajdar, Y.-C. Wang, S. Sachdev, and Z. Y. Meng, Triangular lattice quantum dimer model with variable dimer density, *Nature communications* **13**, 5799 (2022).
- [86] B.-B. Mao, Y.-M. Ding, Z. Wang, S. Hu, and Z. Yan, Sampling reduced density matrix to extract fine levels of entanglement spectrum and restore entanglement hamiltonian, *Nature Communications* **16**, 2880 (2025).
- [87] Z. Wang, Z. Wang, B.-B. Mao, and Z. Yan, Generalized reduced-density-matrix quantum monte carlo gives access to more, arXiv preprint arXiv:2603.10948 (2026).
- [88] B.-B. Mao, Z. Wang, B.-B. Chen, and Z. Yan, Detecting the emergent continuous symmetry of criticality via a subsystem's entanglement spectrum, *Physical Review Letters* **136**, 046401 (2026).
- [89] K. Binder, Critical properties from monte carlo coarse graining and renormalization, *Phys. Rev. Lett.* **47**, 693 (1981).
- [90] S. J. Garratt, Z. Weinstein, and E. Altman, Measurements conspire nonlocally to restructure critical quantum states, *Phys. Rev. X* **13**, 021026 (2023).
- [91] G. Delfino and P. Grinza, Universal ratios along a line of critical points. the ashkin–teller model, *Nuclear Physics B* **682**, 521 (2004).
- [92] J. Simon, W. S. Bakr, R. Ma, M. E. Tai, P. M. Preiss, and M. Greiner, Quantum simulation of antiferromagnetic spin chains in an optical lattice, *Nature* **472**, 307 (2011).
- [93] H. Labuhn, D. Barredo, S. Ravets, S. de Léséleuc, T. Macrì, T. Lahaye, and A. Browaeys, Tunable two-dimensional arrays of single rydberg atoms for realizing quantum ising models, *Nature* **534**, 667 (2016).
- [94] M. Ware, G. Ribeill, D. Ristè, C. A. Ryan, B. Johnson, and M. P. da Silva, Experimental pauli-frame randomization on a superconducting qubit, *Phys. Rev. A* **103**, 042604 (2021).
- [95] H. Lu, C. Liu, D.-S. Wang, L.-K. Chen, Z.-D. Li, X.-C. Yao, L. Li, N.-L. Liu, C.-Z. Peng, B. C. Sanders, Y.-A. Chen, and J.-W. Pan, Experimental quantum channel simulation, *Phys. Rev. A* **95**, 042310 (2017).
- [96] A. Chiuri, V. Rosati, G. Vallone, S. Pádua, H. Imai, S. Giacomini, C. Macchiavello, and P. Mataloni, Experimental realization of optimal noise estimation for a general pauli channel, *Phys. Rev. Lett.* **107**, 253602 (2011).
- [97] S. Wang, T. G. Kiely, D. Tell, J. Obermeyer, M. Barendregt, P. Bojović, P. M. Preiss, A. Sarma, T. Franz, M. P. A. Fisher, C. Xu, and I. Bloch, Observation of strong-to-weak spontaneous symmetry breaking in a dephased fermi gas (2026), arXiv:2604.16137 [cond-mat.quant-gas].
- [98] A. J. Daley, H. Pichler, J. Schachenmayer, and P. Zoller, Measuring entanglement growth in quench dynamics of bosons in an optical lattice, *Phys. Rev. Lett.* **109**, 020505 (2012).
- [99] R. Islam, R. Ma, P. M. Preiss, M. Eric Tai, A. Lukin, M. Rispoli, and M. Greiner, Measuring entanglement entropy in a quantum many-body system, *Nature* **528**, 77 (2015).
- [100] T. Brydges, A. Elben, P. Jurcevic, B. Vermersch, C. Maier, B. P. Lanyon, P. Zoller, R. Blatt, and C. F. Roos, Probing rényi entanglement entropy via randomized measurements, *Science* **364**, 260 (2019), <https://www.science.org/doi/pdf/10.1126/science.aau4963>.
- [101] R. G. Melko, A. B. Kallin, and M. B. Hastings, Finite-size scaling of mutual information in monte carlo simulations: Application to the spin- $\frac{1}{2}$   $xxz$  model, *Phys. Rev. B* **82**, 100409 (2010).
- [102] R. R. P. Singh, M. B. Hastings, A. B. Kallin, and R. G. Melko, Finite-temperature critical behavior of mutual information, *Phys. Rev. Lett.* **106**, 135701 (2011).
- [103] J. D'Emidio, Entanglement entropy from nonequilibrium work, *Phys. Rev. Lett.* **124**, 110602 (2020).
- [104] Y.-M. Ding, J.-S. Sun, N. Ma, G. Pan, C. Cheng, and Z. Yan, Reweight-annealing method for evaluating the partition function via quantum monte carlo calculations, *Phys. Rev. B* **110**, 165152 (2024).
- [105] J. D'Emidio and A. W. Sandvik, Entanglement entropy and deconfined criticality: Emergent so(5) symmetry and proper lattice bipartition, *Phys. Rev. Lett.* **133**, 166702 (2024).
- [106] Z. Wang, Z. Wang, Y.-M. Ding, B.-B. Mao, and Z. Yan, Bipartite reweight-annealing algorithm of quantum monte carlo to extract large-scale data of entanglement entropy and its derivative, *Nature Communications* **16**, 5880 (2025).
- [107] P. S. Tarabunga and Y.-M. Ding, Bell sampling in quantum monte carlo simulations, *Phys. Rev. Lett.* **135**, 200403 (2025).
- [108] Y.-M. Ding, Y. Tang, Z. Wang, Z. Wang, B.-B. Mao, and Z. Yan, Tracking the variation of entanglement rényi negativity: A quantum monte carlo study, *Phys. Rev. B* **111**, L241108 (2025).
- [109] R. Ma, Exploring critical systems under measurements and decoherence via keldysh field theory (2023), arXiv:2304.08277 [quant-ph].
- [110] K.-L. Cai and M. Cheng, Entanglement negativity in

decohered topological states (2026), [arXiv:2602.16597 \[cond-mat.str-el\]](#).

- [111] T.-C. Lu, Disentangling transitions in topological order induced by boundary decoherence, *Phys. Rev. B* **110**, 125145 (2024).
- [112] Z. Wang, R. Fan, T. Wang, S. J. Garratt, and E. Altman, Fractional quantum Hall states under density decoherence, [arXiv \(2025\)](#), [2510.08490](#).
- [113] Z. Weinstein and S. J. Garratt, [Intrinsic error thresholds in nearly critical toric codes](#) (2026), [arXiv:2603.14098 \[cond-mat.stat-mech\]](#).
- [114] Y.-M. Ding, Data for "strong-to-weak spontaneous symmetry breaking in a (2+1)d transverse-field ising model under decoherence", [10.5281/zenodo.19363042](#) (2026).
- [115] Z. Komargodski and D. Simmons-Duffin, The Random-Bond Ising Model in 2.01 and 3 Dimensions, *J. Phys. A* **50**, 154001 (2016), [arXiv:1603.04444 \[hep-th\]](#).
- [116] S. El-Showk, M. F. Paulos, D. Poland, S. Rychkov, D. Simmons-Duffin, and A. Vichi, Solving the 3d ising model with the conformal bootstrap ii.  $c$ -minimization and precise critical exponents, *Journal of Statistical Physics* **157**, 869 (2014).
- [117] W. Zhu, C. Han, E. Huffman, J. S. Hofmann, and Y.-C. He, Uncovering conformal symmetry in the 3d ising transition: State-operator correspondence from a quantum fuzzy sphere regularization, *Phys. Rev. X* **13**, 021009 (2023).
- [118] B. B. Beard and U.-J. Wiese, Simulations of discrete quantum systems in continuous euclidean time, *Phys. Rev. Lett.* **77**, 5130 (1996).
- [119] N. Kawashima and K. Harada, Recent developments of world-line monte carlo methods, *Journal of the Physical Society of Japan* **73**, 1379 (2004).
- [120] R. H. Swendsen and J.-S. Wang, Nonuniversal critical dynamics in monte carlo simulations, *Phys. Rev. Lett.* **58**, 86 (1987).
- [121] Y. Aoun, M. Dober, and A. Glazman, Phase Diagram of the Ashkin–Teller Model, *Commun. Math. Phys.* **405**, 37 (2024).

## END MATTER

### Weak symmetry and the Rényi-2 linear order correlator in the doubled space

To illustrate that  $C^{(1)}$  may not be a faithful diagnostic of weak symmetry breaking in the mixed state, we construct a diagonal density matrix in the local  $Z$  basis:

$$\rho = \frac{1}{4} \left( |0\rangle^{\otimes N} \langle 0|^{\otimes N} + |1\rangle^{\otimes N} \langle 1|^{\otimes N} \right) + \frac{1}{4M} \sum_{\alpha=1}^M \left( |\psi_{\alpha}\rangle \langle \psi_{\alpha}| + X |\psi_{\alpha}\rangle \langle \psi_{\alpha}| X \right), \quad (10)$$

where  $X := \prod_i X_i$ , and  $\{|\psi_{\alpha}\rangle\}$  satisfy  $Z_i Z_j |\psi_{\alpha}\rangle = -|\psi_{\alpha}\rangle$ . By construction,  $\rho$  is normalized and has a global weak  $\mathbb{Z}_2$  symmetry.

A direct calculation gives  $C^{(0)} = 0$  but  $C^{(1)} = (M - 1)/(M + 1)$ . Thus, for  $M > 1$ ,  $C^{(1)} \neq 0$  despite  $C^{(0)} = 0$ ,

showing that  $C^{(1)}$ , while natural as a linear order parameter at the Choi-state level, does not provide a faithful diagnostic of weak symmetry breaking in mixed states.

### Stability of the conventional ferromagnetic order under decoherence

Here we clarify why the ground-state ordered region  $J > J_c$  remains conventionally ferromagnetic under the decoherence channel (1). For the linear correlator  $C_{xy}^{(0)}(\rho) = \text{Tr}(\rho Z_x Z_y)$ , the bond operator  $Z_i Z_j$  in the channel (1) commutes with  $Z_x Z_y$ . Therefore, each local channel leaves the linear correlator unchanged:

$$C_{xy}^{(0)}(\mathcal{E}_{\langle ij \rangle}[\rho_0]) = C_{xy}^{(0)}(\rho_0). \quad (11)$$

Applying this result successively to all other local channels gives

$$C_{xy}^{(0)}(\mathcal{E}[\rho_0]) = C_{xy}^{(0)}(\rho_0), \quad \mathcal{E} = \prod_{\langle ij \rangle} \mathcal{E}_{\langle ij \rangle}. \quad (12)$$

Hence, if the original TFIM ground state is already ordered when  $J > J_c$ , then

$$\lim_{|x-y| \rightarrow \infty} C_{xy}^{(0)}(\mathcal{E}[\rho_0]) = \lim_{|x-y| \rightarrow \infty} C_{xy}^{(0)}(\rho_0) \neq 0. \quad (13)$$

Thus, the decoherence channel cannot restore the symmetry when  $J > J_c$ , since the linear order parameter  $C^{(0)}$  is exactly unchanged.

We further confirm this conclusion numerically by fixing  $J = 0.4 > J_c$  and scanning the decoherence strength  $p$  from 0 to 1. As shown in Fig. 4, the Binder ratios associated with both  $C^{(1)}$  and  $C^{(2)}$  rapidly approach the ordered-region value 1 with increasing system size, and no crossing point is observed. This provides additional evidence that no decoherence-driven phase transition occurs in the conventionally ordered region.

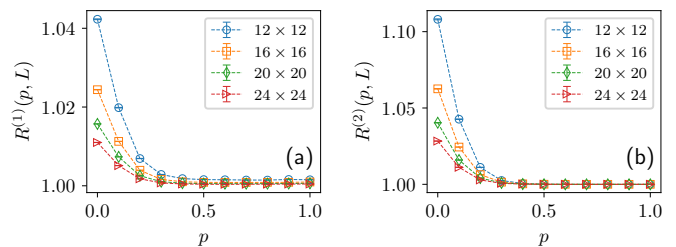


FIG. 4. Fixing  $J = 0.4$ , scanning  $p$ , the corresponding binder ratios of the correlators  $C^{(1)}$  in (a) and  $C^{(2)}$  in (b), respectively.

### Phase transition between R2-SSB and R2-SWSSB

In this subsection, we show a representative example of the numerical results on blue critical boundary

in Fig. 2, associated with  $C^{(1)}$ . We fix  $p = 0.6$  and tune  $J$ . Fig. 5 shows crossings of the Binder ratio  $R^{(1)}$  for different system sizes, from which we extract the critical point  $J_c \approx 0.27$  and the correlation-length exponent  $\nu \approx 0.98 \approx 1$ , consistent with the 2D Ising universality class. This provides further numerical support for the Ising nature of the blue phase boundary discussed in the main text.

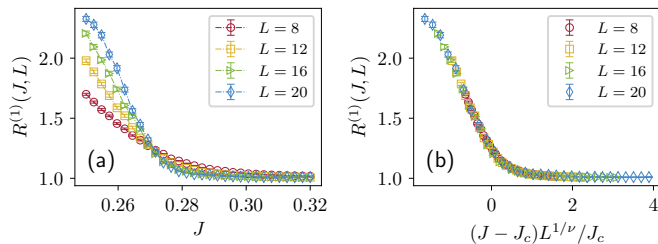


FIG. 5. An example for the blue critical boundary in Fig. 2. At fixed  $p = 0.6$ , we tune  $J$  and evaluate the Binder ratio  $R^{(1)}$ . (a) Crossings of  $R^{(1)}(J, L)$  for different system sizes locate the critical point at  $J_c \approx 0.27$ . (b) Finite-size scaling yields an excellent data collapse with  $\nu \approx 0.98$ , close to the expected Ising value  $\nu = 1$ .

### Decoherence at Ising criticality

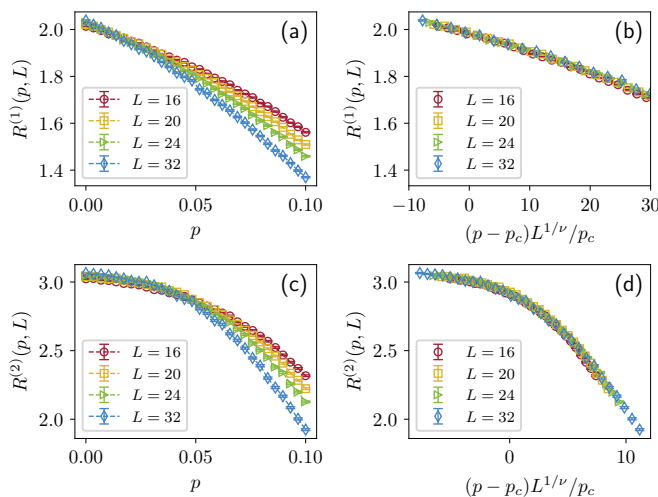


FIG. 6. Binder ratios  $R^{(\alpha)}$  as functions of system size  $L$  and tuning parameters  $J$  and  $p$ . Results for  $\alpha = 1$  are shown in (a, b), and for  $\alpha = 2$  in (c, d). We fix  $J = 0.328474$ . (a, c) show  $R^{(\alpha)}$  versus the decoherence rate  $p$  for different  $L$ , exhibiting crossings that locate the critical points, while (b, d) show the corresponding data collapse using  $\nu = 1.70$ . The crossing points are  $p_c \approx 0.01$  in (a) and  $p_c \approx 0.04$  in (c).

We now analyze the regime in which the bulk is tuned to criticality, such that the defect is coupled to a 3D Ising CFT. In this case, the effective description in terms of a 2D short-range Ashkin-Teller model breaks down due to

the emergence of long-range interactions. We therefore analyze this regime using conformal perturbation theory [115].

The leading relevant perturbation on the defect is given by

$$-\tilde{m} \int d^2x dz \delta(z) (\varepsilon^a + \varepsilon^b), \quad (14)$$

where  $\varepsilon$  denotes the energy-density operator. Given the scaling dimension  $\Delta_\varepsilon \approx 1.41 < 2$  for the 3D Ising universality class [116, 117], this perturbation is relevant. It drives the theory into the R2-SSB phase, breaking  $\mathbb{Z}_2^a \times \mathbb{Z}_2^b$  down to the trivial group. Consequently, the phase transition occurs exactly at  $p = 0$ , characterized by the critical exponent  $\nu = 1/(2 - \Delta_\varepsilon) \approx 1.70$ .

To verify this numerically, we fix  $J = 0.328474 \approx J_c$  [75] and vary  $p$ , measuring both the double-space Rényi-2 linear Binder ratio  $R^{(1)}$  and the Rényi-2 Binder ratio  $R^{(2)}$ . As shown in Fig. 6(a, c), finite-size effects near criticality induce a systematic drift of the crossing points at fixed  $J = J_c$ , yielding  $p_c \approx 0.01$  for  $R^{(1)}$  and  $p_c \approx 0.04$  for  $R^{(2)}$ . Nevertheless, we find that with increasing system size the crossings move consistently toward the expected  $p_c = 0$ .

The finite-size scaling analysis using the theoretical exponent  $\nu = 1.70$  yields a clear and good data collapse [Fig. 6(b), (d)], capturing the overall scaling behavior across the accessible system sizes. This provides strong evidence that the numerical results are consistent with the field-theoretical prediction. Independent fits give  $\nu \approx 2.23$  for  $R^{(1)}$  and  $\nu \approx 1.87$  for  $R^{(2)}$ , with the latter already close to the expected value. The larger deviation in  $R^{(1)}$  can be attributed to stronger finite-size effects and statistical fluctuations. Overall, these results support the expected universality class, with remaining discrepancies attributable to finite-size corrections for system sizes up to  $32 \times 32$ .

### Continuously varying critical exponents

In this subsection, we present representative numerical results for the overlapping critical boundary in Fig. 2, separating the strongly symmetric and R2-SSB phases, where the critical behavior is expected to exhibit continuously varying exponents.

We fix  $p = 0.1$  and  $p = 0.2$ , and tune  $J$  to probe the phase transitions, as shown in Fig. 7. For  $p = 0.1$  and  $p = 0.2$ , crossings of the Binder ratio  $R^{(1)}(J, L)$  locate the transition points at  $J_c \approx 0.327$  and  $J_c \approx 0.318$ , respectively. Performing finite-size scaling around these points yields correlation-length exponents  $\nu \approx 0.658$  and  $\nu \approx 0.691$ , demonstrating a clear dependence of the critical exponent on  $p$  and providing direct numerical evidence for continuously varying criticality along this phase boundary.

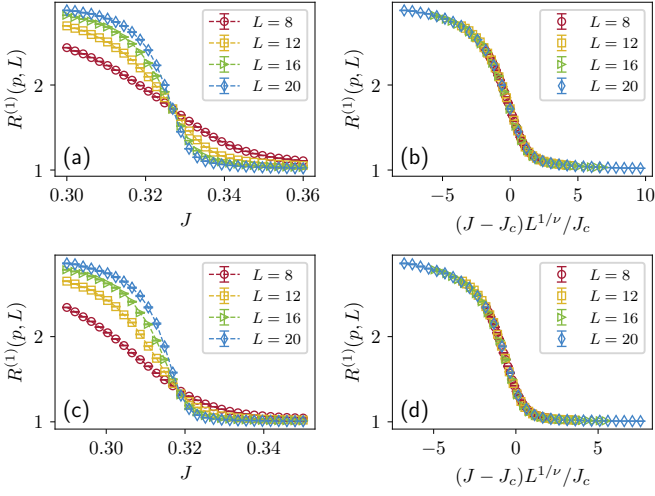


FIG. 7. Representative examples along the overlapping critical boundary separating the strongly symmetric and R2-SSB phases in Fig. 2. At fixed  $p = 0.1$  [(a), (b)] and  $p = 0.2$  [(c), (d)], we tune  $J$  and evaluate the Binder ratio  $R^{(1)}$ . (a), (c) Crossings of  $R^{(1)}(J, L)$  for different system sizes locate the critical points at  $J_c \approx 0.327$  ( $p = 0.1$ ) and  $J_c \approx 0.318$  ( $p = 0.2$ ). (b), (d) Finite-size scaling yields good data collapse with  $\nu \approx 0.658$  ( $p = 0.1$ ) and  $\nu \approx 0.691$  ( $p = 0.2$ ), demonstrating continuously varying critical exponents along this phase boundary.

# Supplemental Material for “Strong-to-Weak Spontaneous Symmetry Breaking in a (2 + 1)D Transverse-Field Ising Model under Decoherence”

Yi-Ming Ding, Yuxuan Guo, Zhen Bi, and Zheng Yan

## STRONG-TO-WEAK SPONTANEOUS SYMMETRY BREAKING

In this section, we briefly review the notions of weak and strong symmetry for mixed states and quantum channels. Building on these definitions, we introduce the diagnostic observables used in the main text in the next section.

The distinction is essential for mixed states: a density matrix may be invariant as an operator even when its decomposition involves components from different symmetry sectors. This gives rise to the possibility of strong-to-weak spontaneous symmetry breaking (SWSSB), where the strong symmetry is spontaneously broken while the weak symmetry remains intact.

Specifically, let  $G$  be an internal symmetry group represented on the Hilbert space  $\mathcal{H}$  by unitary operators  $U_g$ , with  $g \in G$ . For convenience, we define the following superoperators:

$$\mathcal{L}_g(\rho) := U_g \rho, \quad \mathcal{R}_g(\rho) := \rho U_g^\dagger, \quad \mathcal{U}_g(\rho) := U_g \rho U_g^\dagger. \quad (\text{S1})$$

Here  $\mathcal{L}_g$  and  $\mathcal{R}_g$  are the left and right symmetry actions, while  $\mathcal{U}_g = \mathcal{L}_g \circ \mathcal{R}_g$  is the usual adjoint action.

Two mixed-state symmetries are defined as follows:

- A mixed state  $\rho$  has a *weak*  $G$  symmetry if it is invariant under the adjoint action,

$$\mathcal{U}_g(\rho) = U_g \rho U_g^\dagger = \rho, \quad \forall g \in G. \quad (\text{S2})$$

Equivalently,  $[\rho, U_g] = 0$  for all  $g \in G$ ;

- A mixed state  $\rho$  has a *strong*  $G$  symmetry if the symmetry acts separately on the left and right of  $\rho$ . For the one-dimensional charge sectors relevant to the present work, this condition can be written as

$$\mathcal{L}_g(\rho) = U_g \rho = e^{i\phi_g} \rho, \quad \mathcal{R}_g(\rho) = \rho U_g^\dagger = e^{-i\phi_g} \rho, \quad \forall g \in G, \quad (\text{S3})$$

where  $e^{i\phi_g}$  is a one-dimensional character of  $G$ .

Note that Eq. (S3) immediately implies Eq. (S2), thus strong symmetry is a refinement of weak symmetry. Weak symmetry is therefore an operator- or ensemble-level condition: only the full density matrix is required to be symmetric. Physically, a strongly symmetric mixed state is analogous to a fixed-charge ensemble, while a weakly symmetric mixed state may contain an incoherent mixture of different charge sectors as long as the density matrix as a whole is invariant.

The symmetry properties of a quantum channel are the dynamical counterparts of the state symmetries defined above:

- A quantum channel  $\mathcal{E}$  has a weak  $G$  symmetry if it is covariant under the adjoint action,

$$\mathcal{E} \circ \mathcal{U}_g = \mathcal{U}_g \circ \mathcal{E}, \quad \forall g \in G. \quad (\text{S4})$$

Equivalently,

$$\mathcal{E}(U_g \rho U_g^\dagger) = U_g \mathcal{E}(\rho) U_g^\dagger, \quad \forall \rho, \forall g \in G. \quad (\text{S5})$$

- A quantum channel  $\mathcal{E}$  has a strong  $G$  symmetry if it commutes with the left and right symmetry actions separately,

$$\mathcal{E} \circ \mathcal{L}_g = \mathcal{L}_g \circ \mathcal{E}, \quad \mathcal{E} \circ \mathcal{R}_g = \mathcal{R}_g \circ \mathcal{E}, \quad \forall g \in G. \quad (\text{S6})$$

Equivalently,

$$\mathcal{E}(U_g \rho) = U_g \mathcal{E}(\rho), \quad \mathcal{E}(\rho U_g^\dagger) = \mathcal{E}(\rho) U_g^\dagger, \quad \forall \rho, \forall g \in G. \quad (\text{S7})$$

In our setup, the ground state  $\rho_0$  of the transverse-field Ising model (TFIM) is strongly  $\mathbb{Z}_2$  symmetric under  $X \equiv \prod_i X_i$  in the paramagnetic phase. In the ferromagnetic phase, this strong symmetry is spontaneously broken to the trivial group  $\{e\}$ , which is the ordinary (strong-to-trivial) *spontaneous symmetry breaking (SSB)*. Moreover, one can easily verify that the decoherence channel  $\mathcal{E}$  is itself strongly  $\mathbb{Z}_2$  symmetric according to Eq. (S7). Hence, when acting on a strongly symmetric input state  $\rho_0$ , the decohered state  $\mathcal{E}(\rho_0)$  still formally preserves the strong  $\mathbb{Z}_2$  symmetry.

To illustrate how SWSSB can arise, consider the product-state limit  $J = 0$  of the TFIM and the fully decohered limit  $p = 1$ . The initial ground state is

$$\rho_0 = |+\rangle^{\otimes N} \langle +|^{\otimes N} = \frac{1}{2^N} \prod_{i=1}^N (I_i + X_i), \quad |+\rangle = \frac{|0\rangle + |1\rangle}{\sqrt{2}}, \quad (\text{S8})$$

where  $I_i$  and  $X_i$  are the identity and Pauli- $X$  operators on site  $i$ . The decoherence channel is

$$\mathcal{E} = \prod_{\langle ij \rangle} \mathcal{E}_{\langle ij \rangle}, \quad \mathcal{E}_{\langle ij \rangle}(\rho) = \frac{1}{2} (\rho + Z_i Z_j \rho Z_i Z_j). \quad (\text{S9})$$

This gives the decohered state

$$\rho_+ \equiv \mathcal{E}(\rho_0) = \frac{I + X}{2^N}, \quad I \equiv \prod_i I_i. \quad (\text{S10})$$

To expose its structure, we rewrite Eq. (S10) in the  $Z$  basis. Let  $s \in \{0, 1\}^{\otimes N} \equiv \{\uparrow, \downarrow\}^{\otimes N}$  denote a bit string, and let  $\bar{s}$  denote its globally flipped partner, i.e.,  $|\bar{s}\rangle = X |s\rangle$ . Then

$$\rho_+ \propto \sum_s |\text{Cat}_s\rangle \langle \text{Cat}_s|, \quad |\text{Cat}\rangle_s = \frac{|s\rangle + |\bar{s}\rangle}{\sqrt{2}}. \quad (\text{S11})$$

Thus  $\rho_+$  is a uniform convex mixture of cat states, or equivalently the maximally mixed state within the  $X = +1$  symmetry sector.

Eq. (S11) explains why the formal strong  $\mathbb{Z}_2$  symmetry of  $\rho_+$  is compatible with the behavior of SWSSB. Each  $|\text{Cat}_s\rangle$  is formally symmetric, just like the Ising cat state for describing a quantum ferromagnet

$$|\text{Cat}\rangle = \frac{|0 \cdots 0\rangle + |1 \cdots 1\rangle}{\sqrt{2}}, \quad (\text{S12})$$

which is invariant under the global strong  $\mathbb{Z}_2$  symmetry. In the thermodynamic limit ( $N \rightarrow \infty$ ), however,  $|\text{Cat}\rangle$  is unstable to infinitesimal longitudinal symmetry-breaking fields  $h_l$ , which select a symmetry-broken configuration. Mathematically, this reflects the noncommutativity of the limits,  $\lim_{h_l \rightarrow 0} \lim_{N \rightarrow \infty} \neq \lim_{N \rightarrow \infty} \lim_{h_l \rightarrow 0}$ . Similarly,  $\rho_+$  remains formally strongly symmetric at finite size, but its strong symmetry is spontaneously broken to the weak one in the thermodynamic limit.

We now explain why SWSSB cannot be diagnosed by an ordinary linear correlator. For the SWSSB state  $\rho_+$  in Eq. (S11), one finds

$$C_{ij}^{(0)} = \text{Tr}(\rho_+ Z_i Z_j) = \frac{1}{2^N} [\text{Tr}(Z_i Z_j) + \text{Tr}(X Z_i Z_j)] = 0, \quad (\text{S13})$$

using the fact that every nontrivial Pauli string is traceless. Therefore, as long as the weak symmetry is preserved,  $C_{ij}^{(0)}$  cannot diagnose whether the strong  $\mathbb{Z}_2$  symmetry is broken.

In more general cases, for a symmetry group  $G$ , let  $O_\alpha$  be a local order-parameter multiplet, then it transforms as

$$U_g^\dagger O_\alpha U_g = \sum_\beta R_{\alpha\beta}(g) O_\beta, \quad (\text{S14})$$

where  $R(g)$  is the corresponding representation matrix. If the density matrix has weak symmetry, i.e.,  $U_g \rho U_g^\dagger = \rho$ , then the linear correlator gives

$$C_\alpha^{(0)} = \text{Tr}(\rho O_\alpha) = \text{Tr}(U_g \rho U_g^\dagger O_\alpha) = \sum_\beta R_{\alpha\beta}(g) C_\beta^{(0)}, \quad \forall g \in G. \quad (\text{S15})$$

The vector  $C_\alpha^{(0)}$  must be unchanged by every weak symmetry operation. Averaging over all  $g \in G$  gives

$$C_\alpha^{(0)} = \frac{1}{|G|} \sum_\beta \sum_{g \in G} R_{\alpha\beta}(g) C_\beta^{(0)}. \quad (\text{S16})$$

For a nontrivial irreducible representation, the group average of matrix element  $R_{\alpha\beta}$  vanishes. Hence a weakly symmetric density matrix has  $C_\alpha^{(0)} = 0$  for any nontrivial order parameter. However, this constraint does not apply to nonlinear quantities, including the Rényi-2 observables introduced below.

### RÉNYI-2 OBSERVABLES

Consider the Choi–Jamiołkowski isomorphism [69, 70], which maps operators on the Hilbert space  $\mathcal{H}$  to vectors in the doubled Hilbert space  $\mathcal{H}_a \otimes \mathcal{H}_b^*$ , where the subscripts  $a$  and  $b$  label the two copies. For linear bounded operator  $\rho \in \mathcal{B}(\mathcal{H})$ , with matrix elements  $\rho_{ss'}$  in an orthonormal basis  $\{|s\rangle\}$ ,

$$\rho = \sum_{s,s'} \rho_{ss'} |s\rangle\langle s'| \quad \mapsto \quad |\rho\rangle\rangle = \sum_{s,s'} \rho_{ss'} |s\rangle_a |s'\rangle_b^*, \quad (\text{S17})$$

where  $|\rho\rangle\rangle$  is the Choi state of  $\rho$ , which is a pure state in the doubled space  $\mathcal{H}_a \otimes \mathcal{H}_b^*$ .

We again use the TFIM as a concrete example. In the doubled Hilbert space, the symmetry group is

$$\mathbb{Z}_2^a \times \mathbb{Z}_2^b \rtimes \mathbb{Z}_2^H, \quad (\text{S18})$$

where  $\mathbb{Z}_2^H$  originates from the Hermiticity of the original density matrix  $\rho$  and exchanges the two spaces. This structure leads to the following hierarchy of symmetries for the Choi state  $|\rho\rangle\rangle$ :

$$\mathbb{Z}_2^a \times \mathbb{Z}_2^b \supset \mathbb{Z}_2^{\text{diag}} \supset \{e\}. \quad (\text{S19})$$

Explicitly,

$$\mathbb{Z}_2^a \times \mathbb{Z}_2^b = \{(e^a, e^b), (e^a, g^b), (g^a, e^b), (g^a, g^b)\}, \quad (\text{S20})$$

$$\mathbb{Z}_2^{\text{diag}} = \{(e^a, e^b), (g^a, g^b)\} \cong \mathbb{Z}_2, \quad (\text{S21})$$

with  $(g^{a/b})^2 = e^{a/b}$ .

Since  $|\rho\rangle\rangle$  is a pure state, it can only have a strong symmetry or be symmetry-breaking (trivial symmetry). Moreover, the hierarchy in Eq. (S19) allows the Choi state to realize two levels of strong symmetry, which correspond to different symmetry notions for the original density matrix  $\rho$ :

$$\text{Strong } \mathbb{Z}_2^a \times \mathbb{Z}_2^b \text{ symmetry of } |\rho\rangle\rangle \longleftrightarrow \text{Strong } \mathbb{Z}_2 \text{ symmetry of } \rho, \quad (\text{S22})$$

$$\text{Strong } \mathbb{Z}_2^{\text{diag}} \text{ symmetry of } |\rho\rangle\rangle \longleftrightarrow \text{Weak } \mathbb{Z}_2 \text{ symmetry of } \rho, \quad (\text{S23})$$

$$\text{Complete symmetry-breaking of } |\rho\rangle\rangle \longleftrightarrow \text{Complete symmetry-breaking of } \rho. \quad (\text{S24})$$

Here Eq. (S23) corresponds to the *partial* (strong-to-strong) symmetry breaking  $\mathbb{Z}_2^a \times \mathbb{Z}_2^b \longrightarrow \mathbb{Z}_2^{\text{diag}}$  of the Choi state  $|\rho\rangle\rangle$ . For the density matrix  $\rho$ , it is interpreted as the Rényi-2 SWSSB. At the Choi-state level, the natural diagnostic for SWSSB is the Rényi-2 correlator

$$C^{(2)} = \lim_{|i-j| \rightarrow \infty} \frac{\langle\langle \rho | Z_i^a Z_j^a \otimes Z_i^b Z_j^b | \rho \rangle\rangle}{\langle\langle \rho | \rho \rangle\rangle} = \lim_{|i-j| \rightarrow \infty} \frac{\text{Tr}(\rho Z_i Z_j \rho Z_i Z_j)}{\text{Tr}(\rho^2)}. \quad (\text{S25})$$

For the illustrative SWSSB state  $\rho_+$  in Eq. (S11), one finds  $C^{(2)} = 1 \neq 0$ . Together with  $C^{(0)} = 0$  in Eq. (S13), this shows that the strong symmetry is spontaneously broken to a weak symmetry.

By contrast, Eq. (S24) corresponds to ordinary SSB of the pure state  $|\rho\rangle\rangle$ , where even the smaller diagonal subgroup  $\mathbb{Z}_2^{\text{diag}}$  is no longer preserved. **At the Choi-state or Rényi-2 level**, this complete breaking is diagnosed by

$$C^{(1)} = \lim_{|i-j| \rightarrow \infty} \frac{\langle\langle \rho | Z_i^{a/b} Z_j^{a/b} | \rho \rangle\rangle}{\langle\langle \rho | \rho \rangle\rangle} = \lim_{|i-j| \rightarrow \infty} \frac{\text{Tr}(\rho^2 Z_i Z_j)}{\text{Tr}(\rho^2)} \neq 0. \quad (\text{S26})$$

On the other hand, if one considers directly the original density matrix  $\rho$  without relying on the Choi-state viewpoint, then complete symmetry breaking of  $\rho$  should be diagnosed by the conventional linear correlator

$$C^{(0)} = \lim_{|i-j| \rightarrow \infty} \text{Tr}(\rho Z_i Z_j) \neq 0, \quad (\text{S27})$$

This is the faithful diagnostic of ordinary symmetry breaking **at the mixed-state level**. Therefore, one should not assume that the Choi-state diagnostic  $C^{(1)}$ , although natural at the Rényi-2 level, is always fully equivalent to the linear mixed-state diagnostic  $C^{(0)}$ . The counterexample introduced in the End Matter is to illustrate this distinction:  $C^{(1)}$  can diagnose symmetry breaking of the Choi state, but it does not by itself provide a faithful diagnostic of complete (weak) symmetry breaking of the original density matrix.

In practice, both  $C^{(0)}$  and  $C^{(1)}$  should be taken into consideration. More importantly, for the setup considered in our work,  $C^{(1)}$  is not merely a Choi-state diagnostic. It has a natural physical interpretation, as it diagnoses one of the Ising phase transitions in the effective Ashkin–Teller theory.

### DERIVATION OF EQS. (3) AND (4)

The local channel is  $\mathcal{E}_{(ij)} = \sum_k M_k \rho M_k^\dagger$ . Here, we rewrite  $M_k$  defined in Eq. (2) as

$$M_0 = \sqrt{1-p} \mathbb{1}_i \mathbb{1}_j, \quad (\text{S28})$$

$$M_1 = \sqrt{p} \left( |0_i 0_j\rangle \langle 0_i 0_j| + X_i X_j |0_i 0_j\rangle \langle 0_i 0_j| X_i X_j \right), \quad (\text{S29})$$

$$M_2 = \sqrt{p} \left( |0_i 1_j\rangle \langle 0_i 1_j| + X_i X_j |0_i 1_j\rangle \langle 0_i 1_j| X_i X_j \right). \quad (\text{S30})$$

For a computational basis state  $|s\rangle = \otimes_k |s_k\rangle$ , we decompose it as

$$|s\rangle \equiv |s_{ij}\rangle \otimes |s_{\overline{ij}}\rangle, \quad (\text{S31})$$

where

$$|s_{ij}\rangle \equiv |s_i\rangle \otimes |s_j\rangle, \quad |s_{\overline{ij}}\rangle \equiv \otimes_{k \neq i,j} |s_k\rangle. \quad (\text{S32})$$

Accordingly, the density matrix  $\rho_0$  can be expanded as

$$\rho_0 = \sum_{s,s'} \langle s | \rho_0 | s' \rangle |s\rangle \langle s'| = \sum_{s,s'} \langle s_{ij}, s_{\overline{ij}} | \rho_0 | s'_{ij}, s'_{\overline{ij}} \rangle |s_{ij}, s_{\overline{ij}}\rangle \langle s'_{ij}, s'_{\overline{ij}}|. \quad (\text{S33})$$

We first evaluate the contribution from  $M_1$ :

$$\begin{aligned} \frac{1}{p} M_1 \rho_0 M_1^\dagger &= |0_i 0_j\rangle \langle 0_i 0_j| \rho_0 |0_i 0_j\rangle \langle 0_i 0_j| + |0_i 0_j\rangle \langle 0_i 0_j| \rho_0 |1_i 1_j\rangle \langle 1_i 1_j| \\ &\quad + |1_i 1_j\rangle \langle 1_i 1_j| \rho_0 |0_i 0_j\rangle \langle 0_i 0_j| + |1_i 1_j\rangle \langle 1_i 1_j| \rho_0 |1_i 1_j\rangle \langle 1_i 1_j|. \end{aligned} \quad (\text{S34})$$

Using the decomposition above, this can be rewritten as

$$\begin{aligned} \frac{1}{p} M_1 \rho_0 M_1^\dagger &= \sum_{s_{ij} \in \{00,11\}} \sum_{s_{\overline{ij}}, s'_{\overline{ij}}} \langle s_{ij}, s_{\overline{ij}} | \rho_0 | s_{ij}, s'_{\overline{ij}} \rangle |s_{ij}, s_{\overline{ij}}\rangle \langle s_{ij}, s'_{\overline{ij}}| \\ &\quad + \sum_{s_{ij} \in \{00,11\}} \sum_{s_{\overline{ij}}, s'_{\overline{ij}}} \langle s_{ij}, s_{\overline{ij}} | \rho_0 X_i X_j | s_{ij}, s'_{\overline{ij}} \rangle |s_{ij}, s_{\overline{ij}}\rangle \langle s_{ij}, s'_{\overline{ij}}| X_i X_j \\ &\equiv \sum_{s_{ij} \in \{00,11\}} \sum_{s_{\overline{ij}}, s'_{\overline{ij}}} \sum_{W \in \{\mathbb{1}_i \mathbb{1}_j, X_i X_j\}} \langle s_{ij}, s_{\overline{ij}} | \rho_0 W | s_{ij}, s'_{\overline{ij}} \rangle |s_{ij}, s_{\overline{ij}}\rangle \langle s_{ij}, s'_{\overline{ij}}| W. \end{aligned} \quad (\text{S35})$$

Similarly, for  $M_2$  one obtains

$$\frac{1}{p} M_2 \rho_0 M_2^\dagger = \sum_{s_{ij} \in \{01,10\}} \sum_{s_{\overline{ij}}, s'_{\overline{ij}}} \sum_{W \in \{\mathbb{1}_i \mathbb{1}_j, X_i X_j\}} \langle s_{ij}, s_{\overline{ij}} | \rho_0 W | s_{ij}, s'_{\overline{ij}} \rangle |s_{ij}, s_{\overline{ij}}\rangle \langle s_{ij}, s'_{\overline{ij}}| W. \quad (\text{S36})$$

Combining all contributions, we finally arrive at

$$\mathcal{E}_{\langle ij \rangle}[\rho_0] = \sum_k M_k \rho M_k = (1-p)\rho_0 + p \sum_{s_{ij}} \sum_{s_{\bar{i}\bar{j}}, s'_{\bar{i}\bar{j}}} \sum_W \langle s_{ij}, s_{\bar{i}\bar{j}} | \rho_0 W | s_{ij}, s'_{\bar{i}\bar{j}} \rangle | s_{ij}, s_{\bar{i}\bar{j}} \rangle \langle s_{ij}, s'_{\bar{i}\bar{j}} | W, \quad (\text{S37})$$

where  $s_{ij} \in \{0, 1\}^{\otimes 2}$ ,  $s_{\bar{i}\bar{j}}, s'_{\bar{i}\bar{j}} \in \{0, 1\}^{\otimes (N-2)}$ , and  $W \in \{\mathbb{1}_i \mathbb{1}_j, X_i X_j\}$ . Using Eq. (S33), we rewrite Eq. (S37) as

$$\rho \equiv \mathcal{E}_{\langle ij \rangle}[\rho_0] = \sigma_1 + \sigma_2, \quad (\text{S38})$$

where

$$\sigma_1 \equiv \frac{1-p}{2} \sum_s \sum_{s'} \sum_W \langle s | \rho_0 W W | s' \rangle | s \rangle \langle s' |, \quad (\text{S39})$$

$$\begin{aligned} \sigma_2 &\equiv p \sum_{s_{ij}} \sum_{s_{\bar{i}\bar{j}}, s'_{\bar{i}\bar{j}}} \sum_W \langle s_{ij}, s_{\bar{i}\bar{j}} | \rho_0 W | s_{ij}, s'_{\bar{i}\bar{j}} \rangle | s_{ij}, s_{\bar{i}\bar{j}} \rangle \langle s_{ij}, s'_{\bar{i}\bar{j}} | W \\ &= p \sum_s \sum_{s'_{\bar{i}\bar{j}}} \sum_W \langle s | \rho_0 W | s_{ij}, s'_{\bar{i}\bar{j}} \rangle | s \rangle \langle s_{ij}, s'_{\bar{i}\bar{j}} | W. \end{aligned} \quad (\text{S40})$$

### QUANTUM MONTE CARLO ALGORITHM

In this section we describe how to simulate a quantum state  $\rho_0$  under a single local decoherence channel  $\mathcal{E}_{\langle ij \rangle}$ , corresponding to the state in Fig. 1(b), using QMC, provided that the state  $\rho_0$  itself can be simulated by QMC. The generalization to the full channel  $\mathcal{E} = \prod_{\langle ij \rangle} \mathcal{E}_{\langle ij \rangle}$  in Fig. 1(e) is straightforward and therefore omitted for brevity.

For illustrations, we take  $\rho_0 = e^{-\beta H}$  to be the unnormalized Gibbs state of a Hamiltonian  $H$ , which can be obtained from finite-temperature QMC simulations. For sufficiently large  $\beta$ ,  $\rho_0$  approximates the ground state. More generally,  $\rho_0$  may represent a mixed state obtained by tracing out environmental degrees of freedom, and the same implementation of the decoherence channel described below applies as well.

To compute linear observables of  $\rho$ , we introduce the generalized partition function

$$\text{Tr}(\rho) \equiv \text{Tr}(\sigma_1) + \text{Tr}(\sigma_2). \quad (\text{S41})$$

Within QMC, the trace is evaluated by sampling configurations in a generalized configuration space. Therefore,  $\text{Tr}(\rho)$  can be viewed as an extended ensemble composed of two sectors associated with the statistical weights of  $\text{Tr}(\sigma_1)$  and  $\text{Tr}(\sigma_2)$ . By allowing stochastic transitions between these sectors, the simulation dynamically switches between them, so that at any given QMC step, only one of the two contributions needs to be evaluated.

Figs. S1(a) and (b) show the evolution pictures (generalized path integral representations) for  $\text{Tr}(\sigma_1)$  and  $\text{Tr}(\sigma_2)$ , respectively. These diagrams are obtained by contracting the bra and ket indices in Figs. 1(c) and (d), with the time orientation to be counterclockwise without loss of generality. For a fixed  $W$  in each QMC configuration, the spin states propagate along the directed time contour by  $W$  operators and the imaginary-time propagation operator  $\rho_0$ .

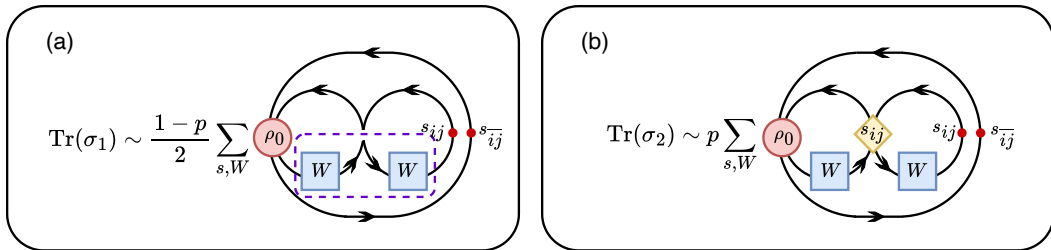


FIG. S1. Graphical representation of (a)  $\text{Tr}(\sigma_1)$  and (b)  $\text{Tr}(\sigma_2)$  in the evolution picture, with propagation from the ket to the bra index in the computational basis.

Consider a configuration in one of the sectors. Note that the spin variables  $s_{ij}$ , starting from the initial time slice, always encounter an even number of operators  $W \in \{\mathbb{1}_i \mathbb{1}_j, X_i X_j\}$  before the application of the imaginary-time

propagation operator  $\rho_0 = e^{-\beta H}$ . Consequently, the spin configuration immediately before and after  $\rho_0$  remains the same. The QMC updates associated with  $\rho_0$  are therefore identical to those used in conventional QMC simulations and can be sampled using standard techniques such as the world-line method (based on the Trotter-Suzuki decomposition) [118, 119] or the stochastic-series-expansion (SSE, based on a Taylor expansion) method [78, 79, 82].

For updates of the  $W$  operators, the two  $W$  operators must be updated simultaneously so that they are either both  $\mathbb{1}_i \mathbb{1}_j$  or both  $X_i X_j$ , according to Eqs. (3) and (4). For example, within the SSE formulation, this constraint can be incorporated into the Swendsen-Wang-like cluster updates (commonly used for the TFIM,  $\mathbb{Z}_2$  lattice gauge theory, Heisenberg model, etc.) [79, 120] with the following additional rules:

- **(Update for  $W$  operators.)** Before growing a cluster to perform the off-diagonal update, each  $W$  operator randomly selects one of the branching choices that determines how the cluster lines enter and exit, as illustrated in Fig. S2. For the two  $W$  operators, there are four possible combinations:  $(A, A)$ ,  $(A, B)$ ,  $(B, A)$ , and  $(B, B)$ . Since in practice  $(A, B)$  and  $(B, A)$  are treated in the same way, as shown Fig. S3, only three distinct cases need to be discussed.

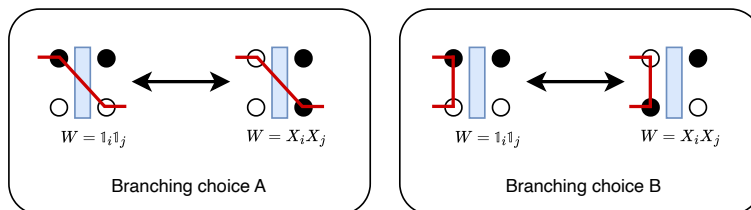


FIG. S2. Two branching choices when a cluster line (red) encounters a  $W$  operator. We follow the standard SSE notation:  $|0\rangle$  is represented by an empty circle and  $|1\rangle$  by a solid circle. The time direction is horizontal, and the blue square denotes the  $W$  operator that propagates the spin states from one side to the other.

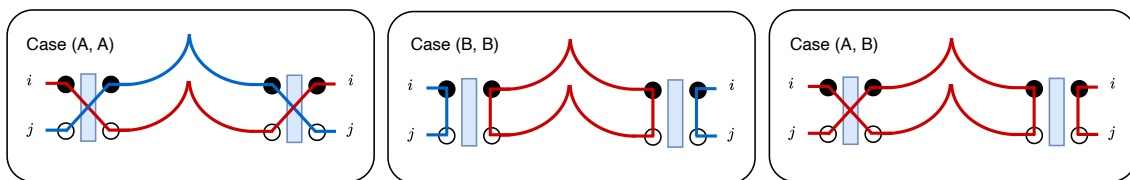


FIG. S3. Three cases in the cluster update of the  $W$  operators on sites  $i$  and  $j$ . The spacetime slice shown corresponds to the region inside the dashed purple square in Fig. S1(a). The red and blue lines denote cluster lines belonging to different clusters.

Here we take  $\text{Tr}(\sigma_1)$  in Fig. S1(a) as an example, and one can similarly discuss  $\text{Tr}(\sigma_2)$ :

- *Case (A, A).* The two  $W$  operators belong to at most two independent clusters, whose cluster lines are denoted by the red and blue lines, respectively. Each cluster is flipped with a probability determined by the Metropolis algorithm, by comparing the configuration weights before and after the flip. For the TFIM, for example, this probability is  $1/2$ .
- *Case (B, B).* There are also at most two independent clusters. Note that if a cluster line enters a spin on the leftmost side, it must correspondingly reappear on the rightmost side to ensure the construction of a complete blue cluster.
- *Case (A, B).* There is only one cluster. This cluster involves all eight spins associated with the two  $W$  operators; therefore, regardless of whether the cluster is flipped, the  $W$  operators remain unchanged in this cluster update.

- **(Sector update.)** To switch between the two sectors, a spin configuration must be compatible with both sectors. In particular, in the  $\text{Tr}(\sigma_2)$  sector the Kronecker tensor imposes the constraint that the spins from the four time directions are identical for sites  $i$  and  $j$ . Therefore, if the spins  $s_{ij}$  from the four time directions are equal, the sector update proceeds as follows:

- If the configuration lies in the sector of  $\text{Tr}(\sigma_1)$ , we switch to  $\text{Tr}(\sigma_2)$  by inserting the Kronecker tensor that identifies the four time directions at lattice sites  $i$  and  $j$ , with probability

$$P(\sigma_1 \rightarrow \sigma_2) = \min \left\{ 1, \frac{1-p}{2p} \right\}. \quad (\text{S42})$$

- If the configuration lies in the sector of  $\text{Tr}(\sigma_2)$ , we switch to  $\text{Tr}(\sigma_1)$  by removing the Kronecker tensor with probability

$$P(\sigma_2 \rightarrow \sigma_1) = \min \left\{ 1, \frac{2p}{1-p} \right\}. \quad (\text{S43})$$

The same framework allows the simulation of  $\text{Tr}(\rho^2)$ , enabling the evaluation of nonlinear two-copy observables such as the Rényi-2 correlator  $C^{(2)}$  and the Rényi-2 linear order correlator  $C^{(1)}$  in the doubled space. This corresponds to sampling an extended ensemble with four sectors

$$\text{Tr}(\rho^2) = \text{Tr}(\sigma_1^2) + \text{Tr}(\sigma_1\sigma_2) + \text{Tr}(\sigma_2\sigma_1) + \text{Tr}(\sigma_2^2). \quad (\text{S44})$$

The associated path-integral representations follow analogously, as shown in Fig. 1(f), and the QMC updates are implemented in the same manner. Because the computational basis is chosen to be the  $Z$  basis, both  $C^{(1)}$  and  $C^{(2)}$  correspond to diagonal measurements when sampling  $\text{Tr}(\rho^2)$ , and can therefore be evaluated with efficiency comparable to conventional QMC simulations.

In closing, we discuss the computational complexity of the QMC scheme introduced here. In our generalized path-integral formulation, the effective imaginary-time extent receives two contributions: the physical inverse temperature  $\beta$  and an additional term proportional to the number of bonds  $N_b = \Theta(L^d)$  arising from  $W$ -operator insertions, where  $d$  is the spatial dimension. As a result, the total imaginary-time length scales as  $\Theta(\max\{\beta, L^d\})$ . Consequently, the cost of a single Monte Carlo sweep is proportional to the spacetime volume (or configuration size)  $\mathcal{V} \sim \mathcal{O}(\max\{\beta, L^d\} L^d)$ . Therefore, the overall computational complexity follows the same scaling as in standard QMC approaches, with  $\mathcal{V}$  replacing the usual spacetime volume, and remains polynomial in system size and inverse square of the error tolerance. Correspondingly, evaluating Rényi-2 observables requires only a constant (factor of two) overhead compared to conventional linear observables, as the simulation involves two replicas of the system.

## DERIVATION OF THE EFFECTIVE 2D DEFECT ACTION

In this section, we explicitly integrate out the massive bulk degrees of freedom to derive the effective two-dimensional action on the defect. We start with the bulk action for a single replica  $\phi$  (omitting the replica index  $a, b$  for brevity), treating the  $\lambda\phi^4$  term as a perturbation. The quadratic part of the bulk action is

$$S_0[\phi] = \int d^2x dz \left[ \frac{1}{2} \partial_i \phi \partial^i \phi + \frac{1}{2} (\partial_z \phi)^2 + \frac{1}{2} m^2 \phi^2 \right], \quad (\text{S45})$$

where  $x^i$  ( $x^i = x, y$ ) denotes the coordinates strictly parallel to the defect, and  $z$  is the perpendicular coordinate. The defect is located at  $z = 0$ .

To integrate out the bulk at tree level, we solve the classical equation of motion (EOM) for the bulk field in the region  $z \neq 0$ :

$$(-\partial_i \partial^i - \partial_z^2 + m^2) \phi(x_i, z) = 0. \quad (\text{S46})$$

Performing a Fourier transform along the defect directions,  $\phi(x_i, z) = \int \frac{d^2k}{(2\pi)^2} e^{ik^i x_i} \tilde{\phi}(k^i, z)$ , the EOM decouples for each momentum mode  $k^\mu$ :

$$(-\partial_z^2 + k^2 + m^2) \tilde{\phi}(k^i, z) = 0, \quad (\text{S47})$$

where  $k^2 = k_i k^i$ . Requiring the field to decay at  $z \rightarrow \pm\infty$ , the solution is given by separation of variables:

$$\tilde{\phi}(k^i, z) = \varphi(k^i) e^{-\sqrt{k^2 + m^2} |z|}, \quad (\text{S48})$$

where  $\varphi(k^i) \equiv \tilde{\phi}(k^i, z = 0)$  is the boundary field strictly confined to the defect.

To evaluate the effective action for the defect field, we substitute the classical solution back into the bare quadratic action  $S_0$ . Using integration by parts, the action can be rewritten as

$$S_0[\phi] = \frac{1}{2} \int d^2x \left[ \int_{-\infty}^{0^-} dz + \int_{0^+}^{\infty} dz \right] [\partial_i(\phi\partial^i\phi) + \partial_z(\phi\partial_z\phi) - \phi(\partial_i\partial^i\phi + \partial_z^2\phi - m^2\phi^2)]. \quad (\text{S49})$$

Since the classical profile strictly satisfies the EOM  $(-\partial_i\partial^i - \partial_z^2 + m^2)\phi = 0$  in the bulk ( $z \neq 0$ ), the last term in the integrand vanishes identically. Assuming the field decays to zero at  $z \rightarrow \pm\infty$ , the integration over  $z$  leaves only the boundary terms at the defect  $z = 0$ :

$$S_0[\phi] = \frac{1}{2} \int d^2x [\phi(x_i, 0)\partial_z\phi(x_i, 0^-) - \phi(x_i, 0)\partial_z\phi(x_i, 0^+)]. \quad (\text{S50})$$

Transforming to momentum space along the defect directions, we use the classical profile  $\tilde{\phi}(k^i, z) = \varphi(k^i)e^{-\sqrt{k^2+m^2}|z|}$ . The normal derivatives at the two sides of the defect are

$$\partial_z\tilde{\phi}(k^i, 0^+) = -\sqrt{k^2+m^2}\varphi(k^i), \quad (\text{S51})$$

$$\partial_z\tilde{\phi}(k^i, 0^-) = +\sqrt{k^2+m^2}\varphi(k^i). \quad (\text{S52})$$

Substituting these derivatives back into the boundary action, the discontinuity of the derivative across  $z = 0$  yields a factor of  $2\sqrt{k^2+m^2}$ , which precisely cancels the  $1/2$  prefactor. Thus, we obtain the effective quadratic action for the boundary field  $\varphi$ :

$$S_{\text{eff}}^{(0)}[\varphi] = \int \frac{d^2k}{(2\pi)^2} \varphi(-k^i)\sqrt{k^2+m^2}\varphi(k^i). \quad (\text{S53})$$

In the trivial bulk phase where  $m > 0$ , the bulk correlation length  $\xi = 1/m$  is finite. For low-energy fluctuations on the defect ( $k \ll m$ ), we can expand the non-local kinetic kernel as  $\sqrt{k^2+m^2} \approx m + \frac{k^2}{2m} + \mathcal{O}(k^4)$ . Transforming back to real space, the effective quadratic action becomes local:

$$S_{\text{eff}}^{(0)}[\varphi] \approx \int d^2x \left[ \frac{1}{2m}\partial_i\varphi\partial^i\varphi + m\varphi^2 \right]. \quad (\text{S54})$$

To account for the bulk interactions, we evaluate the tree-level contribution of the bulk  $\lambda\phi^4$  term using the low-energy classical profile  $\phi(x^i, z) \approx \varphi(x^i)e^{-m|z|}$ . This approximation is equivalent to neglecting derivative interactions generated by the integration over the bulk, which are strictly irrelevant in the renormalization group sense and do not affect the low-energy universal behavior. Integrating over the perpendicular coordinate  $z$  yields

$$\int d^2x \int_{-\infty}^{\infty} dz \lambda (\varphi(x^i)e^{-m|z|})^4 = \int d^2x \frac{\lambda}{2m} \varphi^4(x^i). \quad (\text{S55})$$

Physically, the factor of  $1/m$  reflects the bulk correlation length  $\xi$ , indicating that only the bulk degrees of freedom within a distance  $\xi$  from the defect effectively participate in the interaction.

Here we derive the effective boundary action  $S_{\text{int}}[\phi_a, \phi_b]$  from the microscopic interaction  $V_{\text{int}} = 2\delta(z)u \sum_{\langle i,j \rangle} Z_i^a Z_j^a Z_i^b Z_j^b$ , where  $u \equiv \tanh^{-1}[p/(2-p)]$ .

In the continuum limit, the lattice spin operator  $Z_i$  maps to the scalar field  $\phi(x)$ . Using the operator product expansion (OPE), the nearest-neighbor spin product can be expanded in terms of the identity and the energy density operator  $\epsilon(x) \propto \phi^2(x)$ . Thus, we write the coarse-grained bond operator as  $Z_i Z_j \simeq C_0 + C_1\phi^2(x)$ , with  $C_{0,1}$  being non-universal constants. Applying this to both replicas  $a$  and  $b$ , the four-spin interaction becomes:

$$Z_i^a Z_j^a Z_i^b Z_j^b \simeq C_0^2 + C_0 C_1 (\phi_a^2 + \phi_b^2) + C_1^2 \phi_a^2 \phi_b^2. \quad (\text{S56})$$

Taking the continuum limit  $\sum_{\langle i,j \rangle} \rightarrow \frac{1}{a^2} \int d^2x$  and dropping the trivial constant shift  $C_0^2$ , the continuous interaction action  $S_{\text{int}} = - \int dz V_{\text{int}}$  takes the form:

$$S_{\text{int}} \simeq -\frac{2u}{a^2} \int d^2x dz \delta(z) [C_0 C_1 (\phi_a^2 + \phi_b^2) + C_1^2 \phi_a^2 \phi_b^2]. \quad (\text{S57})$$

Comparing this with the phenomenological 2D Ashkin-Teller boundary action,

$$S_{\text{int}}[\phi_a, \phi_b] = - \int d^2x dz \delta(z) [\tilde{m} (\phi_a^2 + \phi_b^2) + t \phi_a^2 \phi_b^2], \quad (\text{S58})$$

we can explicitly match the coefficients to find  $\tilde{m} = 2C_0C_1u$  and  $t = 2C_1^2u$ .

To bring the effective action into the standard canonical form, we rescale the boundary field as  $\varphi \rightarrow \sqrt{m}\varphi$ , which normalizes the kinetic term to  $\frac{1}{2}\partial_i\varphi\partial^i\varphi$ . Under this rescaling, the effective quartic coupling becomes  $\tilde{\lambda} = \lambda m/2$ . Restoring the replica indices  $a, b$ , we arrive at the full effective 2D action:

$$S_{\text{eff}}[\varphi^a, \varphi^b] = \int d^2x \left[ \sum_{\alpha=a,b} \frac{1}{2} \left( \partial_i\varphi_\alpha\partial^i\varphi_\alpha + m_{\text{eff}}^2\varphi_\alpha^2 + \tilde{\lambda}\varphi_\alpha^4 \right) - \tilde{t}\varphi_a^2\varphi_b^2 \right], \quad (\text{S59})$$

where  $m_{\text{eff}}^2 = m(2m - \tilde{m})$  incorporates the bare mass and the defect potential  $\tilde{m}$ ,  $\tilde{t} = tm^2$ . This is exactly the continuum field theory of the 2D Ashkin-Teller model.

Based on the effective 2D Ashkin-Teller action derived above, we can understand the phase diagram using Landau Ginzburg mean-field theory. The exact phase diagram can be found in [121], where, upon a 90° rotation, it matches our results precisely. Assuming uniform field configurations, the Landau free energy density is given by the potential terms of the effective action:

$$f(\varphi_a, \varphi_b) = \frac{1}{2}m_{\text{eff}}^2(\varphi_a^2 + \varphi_b^2) + \frac{1}{2}\tilde{\lambda}(\varphi_a^4 + \varphi_b^4) - \tilde{t}\varphi_a^2\varphi_b^2 + O(\varphi_a^3\varphi_b^3), \quad (\text{S60})$$

The ground state is determined by minimizing the free energy density. The extremum conditions  $\partial f/\partial\varphi_a = 0$  and  $\partial f/\partial\varphi_b = 0$  yield the equations of state:

$$\varphi_a(m_{\text{eff}}^2 + 2\tilde{\lambda}\varphi_a^2 - 2\tilde{t}\varphi_b^2) = 0, \quad (\text{S61})$$

$$\varphi_b(m_{\text{eff}}^2 + 2\tilde{\lambda}\varphi_b^2 - 2\tilde{t}\varphi_a^2) = 0. \quad (\text{S62})$$

By solving these equations, we identify three distinct physical regimes, which perfectly correspond to the phases observed in our QMC simulations:

**1. Trivial Symmetric Phase:** When  $m_{\text{eff}}^2 > 0$  and  $\tilde{\lambda} > \tilde{t}$ , the only real solution is the trivial vacuum:

$$\langle\varphi_a\rangle = \langle\varphi_b\rangle = 0. \quad (\text{S63})$$

In this regime, the system is in the strongly symmetric phase, and no symmetry is broken. This corresponds to the region where both the TFIM  $J$  and the decoherence strength  $p$  are small.

**2. R2-SSB Phase:** When  $m_{\text{eff}}^2 < 0$ , the trivial vacuum becomes unstable. If the inter-replica coupling  $t$  is positive and relatively small, the system prefers to develop nonzero vacuum expectation values (VEVs) for both replicas simultaneously to minimize the  $-t\varphi_a^2\varphi_b^2$  interaction. The minimum occurs at:

$$\langle\varphi_a\rangle^2 = \langle\varphi_b\rangle^2 = \frac{-m_{\text{eff}}^2}{2\tilde{\lambda} - 2\tilde{t}} = \frac{\tilde{m} - 2m}{\lambda - 2tm}. \quad (\text{S64})$$

In this phase, both  $\langle\varphi_a\rangle \neq 0$  and  $\langle\varphi_b\rangle \neq 0$ , which implies that the  $\mathbb{Z}_2^a \times \mathbb{Z}_2^b$  symmetry is completely broken down to the trivial group. Both  $C^{(1)}$  and  $C^{(2)}$  are nonzero.

Crucially, the ferromagnetic phase is stable only when the inter-replica coupling satisfies  $t < \lambda/2m$ . Near the bulk critical point ( $J \rightarrow J_c$ ), the small mass gap  $m$  yields a large  $t$ , stabilizing this phase over a wide range of  $p$ . Conversely, deeper in the trivial phase (large  $m$ ), achieving negative  $m_{\text{eff}}^2$  requires a large decoherence strength  $p$ . Since  $t$  grows monotonically with  $p$ , it inevitably exceeds  $\lambda$ , violating the stability condition. Consequently, for sufficiently small  $J$ , the ferromagnetic phase is entirely preempted, and the system transitions directly into the Baxter phase.

**3. R2-SWSSB phase:** As the decoherence strength  $p$  increases, the inter-replica coupling  $t$  becomes sufficiently large. In the Ashkin-Teller model, a large  $t$  renders the ferromagnetic phase unstable, as it strongly binds the fluctuations of the two replicas. Consequently, the naive Landau-Ginzburg description is not positive definite and hence becomes inadequate. To properly capture the physics in this regime, one must include higher-order interaction terms and consider the composite field  $\sigma \sim \varphi_a\varphi_b$  as the relevant order parameter. In this phase, the strong inter-replica coupling prevents the individual fields from acquiring a vacuum expectation value ( $\langle\varphi_a\rangle = \langle\varphi_b\rangle = 0$ ), but their composite operator acquires a nonzero expectation value:

$$\langle\varphi_a\varphi_b\rangle \neq 0. \quad (\text{S65})$$

This composite order parameter breaks the full  $\mathbb{Z}_2^a \times \mathbb{Z}_2^b$  symmetry but strictly preserves the diagonal subgroup  $\mathbb{Z}_2^{\text{diag}}$  (under which  $\varphi_a \rightarrow -\varphi_a$  and  $\varphi_b \rightarrow -\varphi_b$  simultaneously). Consequently, the linear correlator vanishes ( $C^{(1)} = 0$ ), while  $C^{(2)} \neq 0$ , marking the hallmark of the SWSSB phase.